

# OptMap: Geometric Map Distillation via Submodular Maximization

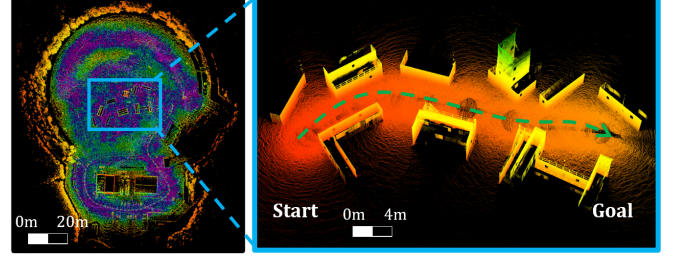
David Thorne<sup>1</sup>, Nathan Chan<sup>1</sup>, Christa S. Robison<sup>2</sup>, Philip R. Osteen<sup>2</sup>, Brett T. Lopez<sup>1</sup>

**Abstract**—Autonomous robots rely on geometric maps to inform a diverse set of perception and decision-making algorithms. As autonomy requires reasoning and planning on multiple scales of the environment, each algorithm may require a different map for optimal performance. Light Detection And Ranging (LiDAR) sensors generate an abundance of geometric data to satisfy these diverse requirements, but selecting informative, size-constrained maps is computationally challenging as it requires solving an NP-hard combinatorial optimization. In this work we present OptMap: a geometric map distillation algorithm which achieves real-time, application-specific map generation via multiple theoretical and algorithmic innovations. A central feature is the maximization of set functions that exhibit diminishing returns, i.e., submodularity, using polynomial-time algorithms with provably near-optimal solutions. We formulate a novel submodular reward function which quantifies informativeness, reduces input set sizes, and minimizes bias in sequentially collected datasets. Further, we propose a dynamically reordered streaming submodular algorithm which improves empirical solution quality and addresses input order bias via an online approximation of the value of all scans. Testing was conducted on open-source and custom datasets with an emphasis on long-duration mapping sessions, highlighting OptMap’s minimal computation requirements. Open-source ROS1 and ROS2 packages are available and can be used alongside any LiDAR SLAM algorithm.

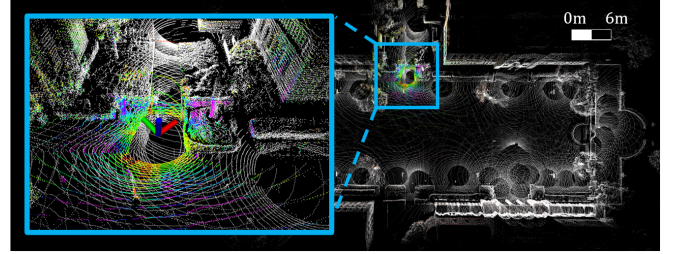
**Index Terms**—Mapping, Submodular Optimization, Formal Methods in Robotics and Automation, Field Robotics

## I. INTRODUCTION

MODERN autonomous systems use a modular software architecture with separate algorithms for perceiving the environment, planning collision-free paths, estimating vehicle motion, and making higher-level decisions to complete their tasks. Many of these algorithms depend on geometric information about the environment to function properly. As a result, their performance and processing time can vary greatly depending on the quality of the geometric data. For example, trajectory planners use geometric maps to plan collision-free paths, but the density of geometric data is critical for balancing real-time replanning requirements against reliable collision detection. This trade-off is best served by dense geometric maps that specifically capture the intended trajectory corridor (Fig. 1a). In contrast, localization entails aligning a source and reference point cloud, a process best served by using a sparse and global reference point cloud to minimize computation time while maximizing alignment accuracy (Fig. 1b). It quickly becomes clear that using *one geometric map* for both algorithms hinders the overall system performance, and



(a) OptMap application map for trajectory planning (right). Map is dense while remaining efficient as only points near the intended trajectory are returned.



(b) OptMap application map for localization (white). One-shot global localization requires a sparse global map with coverage to identify all possible poses such as the scan indicated in the left inset.

Fig. 1: OptMap is a geometric map distillation algorithm which provides size-constrained, informative geometric maps for real-time autonomy algorithms. The two examples above demonstrate OptMap’s flexibility in providing application-specific maps with different requirements.

highlights the demand for an algorithm capable of actively building relevant maps for each application. Designing such an algorithm is challenging because geometric perception sensors (e.g., RGB-D, LiDAR) produce large volumes of data, making any formal method for generating application-specific maps computationally demanding. The ideal algorithm should select informative maps from a set of millions of geometric points subject to dynamic time, position, and size constraints in real-time for safe autonomy. We call this problem *geometric map distillation*, because essential information gathered by perception sensors is extracted to create a compact, application-specific map of maximum utility.

Formally, geometric map distillation is a combinatorial optimization problem that aims to maximize the informativeness of the output map. Point cloud informativeness can be stated using metrics such as the amount of redundant or overlapping information, but efficiently solving combinatorial optimization problems with tight suboptimality bounds using these metrics is challenging. Such optimizations are in part difficult because each overlap comparison is computationally expensive. Previous research sought to simplify overlap calculations by learning to encode point clouds as compact descriptor vectors where the distance between descriptors corresponds to the degree of overlap [1]. Although most descriptors are used for global place recognition [2]–[4], recent work used them

\*This research was sponsored by the DEVCOM Army Research Laboratory (ARL) under SARA CRA W911NF-24-2-0017. Distribution Statement A: Approved for public release; distribution is unlimited.

<sup>1</sup> University of California, Los Angeles, Los Angeles, CA, USA {davidthorne, nchan22, btllopez}@ucla.edu

<sup>2</sup>DEVCOM Army Research Laboratory (ARL), Adelphi, MD, USA. {christa.s.robison, philip.r.osteen}.civ@army.mil

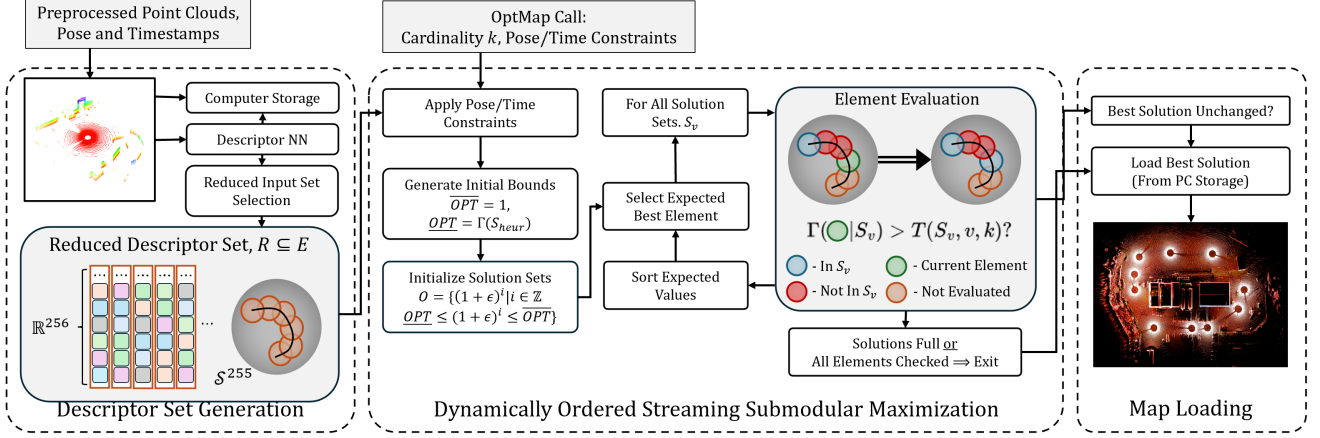


Fig. 2: The OptMap pipeline consists of three stages: (i) descriptor set generation, (ii) dynamically ordered streaming submodular maximization, and (iii) map loading. The first stage occurs either offline or alongside SLAM. Dynamically reordered streaming submodular maximization and map loading take place on parallel threads after receiving an OptMap function call specifying the desired map size as well as additional optional position and time constraints.

to formulate reward functions for summarizing large LiDAR datasets [5]. The key idea of [5] is that submodularity, or the mathematically defined property of diminishing returns, provides efficient algorithms for optimizing subsets of geometric data via metrics such as overlap. The most famous method is the greedy algorithm, which guarantees a  $(1 - \frac{1}{e})$ -suboptimality bound for cardinality constrained submodular problems [6], [7]. A recently developed class of streaming submodular algorithms are pertinent to optimizing over large datasets because they only require a single pass over input datasets [8], [9]. Streaming algorithms have been used to solve problems similar to geometric map distillation such as search engine result generation and image dataset summarization [10], [11] which both aim to select informative subsets from extremely large input sets.

In this paper, we leverage learned descriptors and streaming submodular maximization to develop an algorithm for real-time geometric map distillation called OptMap (Fig. 2). We propose a novel submodular function which assigns weights to elements based on their similarity to prior collected data, allowing for a sequential filtering scheme to remove redundant geometric data and reduce bias towards over-sampled locations. This submodular function is optimized by a streaming submodular maximization algorithm that uses a novel dynamic reordering approach to improve solution quality and address multiple forms of input order bias. Further computation time improvements are derived from an efficient parallel map optimization and loading scheme, and our ability to use the simple geometric relationships between descriptors to derive tight *a priori* solution bounds. We demonstrate OptMap’s ability to distill large LiDAR datasets in several settings, which emphasize high-quality output maps with minimal computational requirements. OptMap is intended to run alongside any ROS1 or ROS2 LiDAR SLAM package, and open-source code (including a lightly modified popular open-source LiDAR SLAM algorithm [12]) is released for efficient testing and development<sup>1</sup>. Although OptMap is designed for LiDAR inputs,

it could be adapted for other forms of geometric perception sensors given equivalent descriptors which compactly encode mutual information. To summarize, the contributions are:

- **Continuous Exemplar-Based Clustering.** Novel submodular function which reduces input set bias and improves evaluation time by discarding redundant scans.
- **Dynamic Reordering.** Addresses sensitivity of streaming submodular algorithms to input order by approximating the marginal values of elements to ensure stream order prioritizes scans with high expected value.
- **Tight Solution Bounds and Parallel Map Loading.** Save optimization and total function time via tight *a priori* optimal solution value bounds, and by loading maps on parallel threads before completing the optimization.
- **Ablation Studies.** Demonstrate OptMap’s ability to find highly informative geometric maps. Studies demonstrate the efficacy of our novel reward function as well as the impact of dynamic reordering when compared with the baseline and multiple heuristic alternatives.
- **Open-Source Code.** Released ROS1 and ROS2 packages. OptMap is meant to be run alongside any LiDAR SLAM algorithm for quick testing and development.

## II. RELATED WORKS

### A. Geometric Maps for Mobile Robots

Key performance metrics for geometric maps include the level of detail and coverage area, the complexity of applying map updates (e.g., loop closures), and the level of flexibility or specificity a map has towards serving multiple functions [13]. Direct geometric maps are generated via the union of point clouds as complete, dense maps which use all collected scans [14], [15] or as lightweight keyframe maps which contain a subset of selected scans [12], [16], [17]. Keyframe maps are easily maintained over long-duration missions as they require less memory and can be updated via pose-graph optimization, but complete maps provide a higher degree of detail. 3D occupancy maps are the most frequently used map type for autonomous planning algorithms [18]. Their primary

<sup>1</sup><https://github.com/vectr-ucla/optmap>

advantages are that they have minimal memory requirements, are easily searched, explicitly model free-space, and are readily generated from multiple fused sensors [19]–[22]. The downside is that they require computationally expensive ray tracing to generate, and can be slow to update in batches (e.g. after a loop closure). Hierarchical graph-based maps can be memory efficient and carry significant detail [23], but are often designed by experts for specific applications and therefore are not well-suited to multiple diverse algorithms.

**Learned Point Cloud Global Descriptors** compress dense point clouds into compact vectors where the distance between descriptors encodes the similarity between point clouds. While a few model-free LiDAR descriptors exist (e.g., [24]), most work in this field has been towards developing neural networks to generate descriptors for global place recognition. Notable recent advances in learned point cloud descriptors include the use of transformers to generate yaw-invariant descriptors [1], [3], and the use of 3D convolutions to enable descriptor generation on sparse point clouds [4]. In [2], the norm of the difference between descriptors can be used to predict the number of points shared between two point clouds.

### B. Submodular Maximization

Submodular maximization is a powerful tool for combinatorial optimization problems which exhibit monotonicity and diminishing returns because it provides efficient solutions to NP-hard problems with tight suboptimality guarantees. The most important result in the field is the proven performance of the greedy algorithm when maximizing non-negative monotone submodular functions subject to cardinality constraints, which achieves a  $1 - \frac{1}{e} \approx 0.63$ -suboptimality bound. This bound is optimal for any algorithm that queries the submodular function a polynomial number of times [6], [7], where greedy requires  $O(kN)$  queries (evaluations) to make a solution of size  $k$  from an input set with  $N$  elements. The computation and memory complexity of the greedy algorithm has been improved several times [25]–[27], with extensions proposed for non-monotone functions [28]–[30]. Advances in submodular theory are frequently applied to computing and machine learning tasks such as dataset summarization, image classification, and search result generation [31]–[33]. Lin et al. [34] provides submodular functions which balance solution representation and diversity for document summarization. Fujishige et al. [35] provides coverage of classical algorithms, common submodular functions, and their constraints.

**Streaming Submodular** algorithms were developed to optimize over large input sets such as video streams or machine learning training datasets. Two approaches to streaming submodular maximization were proposed concurrently by [8] and [36]. Both aimed to maximize a submodular function using only a single evaluation pass or  $O(N)$  queries to the submodular function. The streaming algorithm described in this work is derived from Sieve-Streaming [8] because it is easily recreated and adapted to application-specific reward functions and parameters. The fundamental idea of streaming submodular maximization is that provably near-optimal solutions can be built by identifying valuable elements of the input

set relative to a known optimal solution value. Given that the optimal value is not known *a priori*, multiple solutions are maintained in parallel where each solution has a unique guess at the optimal value. The number of solutions and their relative distance is dictated by a granularity constant  $\epsilon$ . Bounds on the optimal solution value (known or found online) ensure that one of the maintained solutions has a guess that is close to the true optimal, providing a  $(1/2 - \epsilon)$ -suboptimality bound. One often overlooked property of [8] is that the suboptimality guarantee does not require a complete evaluation pass. For example, if all solutions reach the cardinality constraint before the full stream has been evaluated, the algorithm may terminate early and save a significant portion of the required computations.

A major limitation of streaming submodular maximization algorithms is the need to select solutions with limited information, i.e., before evaluating the entire stream. Limited information degrades solution quality because low-quality elements may be included in solutions solely because they appear earlier in the stream, and high-quality elements may be omitted because they are evaluated at the end of the stream. Multiple methods to improve solution quality have been proposed such as [9] which swaps solution elements when a higher quality element is presented. Solution swaps are used in combination with randomized sub-sampling in [10] to achieve near-optimal solutions in expectation with fewer submodular function evaluations. Several methods adopt a pseudo-streaming approach in which batches of elements are considered together (e.g., using a greedy algorithm on subsets of the input set) [11], or where inflated solution sets are refined by post-processing [37]. These methods generally improve solution quality at the cost of either the deterministic nature of the algorithm or additional algorithmic steps which increase computation time. In specific cases where bias in input sets is known *a priori* such as demographic problems, a partition constraint can be used to ensure the solution is not biased [38].

Dynamic submodular maximization algorithms [39]–[42] have a similar motivation to streaming algorithms as they aim to maximize a submodular function through a series of input set insertions and deletions. Dynamic algorithms are a generalized version of streaming algorithms as they do not assume full access to the input set and therefore suffer from worse memory and computation performance.

**Submodular Maximization in Robotics** largely centers on improving the performance and efficiency of autonomous decision making. Many works prove that the underlying problem is submodular as theoretical justification for utilizing the greedy algorithm. Graph optimization is readily formulated as submodular maximization, with notable works in pose graph sparsification [43]–[45], path planning [46], [47], and area search and coverage [48], [49]. Multi-robot coordination has seen numerous advancements where submodularity can guarantee centralized and distributed planning with near-optimal coverage under tight communication constraints [50]–[52]. Submodularity is rarely found in perception algorithms, with notable exceptions in previously mentioned pose graph SLAM [43]–[45], and some works in selecting either visual features [53] or LiDAR scans [5] which best constrain localization.



### III. PRELIMINARY ON SUBMODULARITY

Let  $X$  be a set of elements and  $2^X$  be its power set.

**Definition 1.** A set function  $f : 2^X \rightarrow \mathbb{R}_{\geq 0}$  is said to be *monotonic non-decreasing* if  $f(\emptyset) \geq 0$  and  $f(B) \geq f(A)$  for all subsets  $A \subseteq B \subseteq X$ .

**Definition 2.** A set function  $f : 2^X \rightarrow \mathbb{R}_{\geq 0}$  is *submodular* if for  $A \subseteq B \subseteq X$  and element  $x \in X \setminus B$

$$f(A \cup x) - f(A) \geq f(B \cup x) - f(B). \quad (1)$$

We refer to  $f(A \cup x) - f(A)$  as the marginal value of  $x$  with respect to  $A$  and use the simplified notation  $f(x|A)$ . The intuitive way to understand Definition 2 with respect to submodular maximization is that the marginal value of any element must diminish as the solution increases in size.

Maximization of monotone non-decreasing, submodular functions subject to cardinality constraints is a well-studied problem, with the seminal result being the  $(1 - \frac{1}{e})$ -suboptimality guarantee of the greedy algorithm [6], [7].

**Definition 3.** (*k*-wise information [54]) Given a submodular function  $f$ , the *k*-wise information set is defined as the set of tuples  $\{(S, f(S)) | S \subseteq X, |S| \leq k\}$ . When  $k = 2$ , we refer to this as pairwise information.

Knowing pairwise information for a given function  $f$  and set  $X$  is equivalent to having a look-up table ( $O(1)$  function access) for the value of  $f$  given any solution  $S$  such that  $|S| \leq 2$ . Using pairwise information, an estimated marginal value can be defined as

$$\bar{f}(x|A) = \min_{a \in A} f(x|a) \geq f(x|A). \quad (2)$$

The pairwise marginal value maintains submodularity and monotonicity of  $f$ , and [54] proposes an optimistic greedy algorithm which is shown to produce empirically near-optimal results for several submodular maximization problems. We are interested in pairwise information as a computationally lightweight means for approximating the marginal value of elements with respect to a solution when such marginal values typically would require expensive computations.

#### A. Streaming Submodular Maximization

Streaming submodular algorithms seek to maximize a submodular function using only a single pass over all elements in an input set. If the optimal solution value  $OPT$  were known *a priori*, a solution could be iteratively built by comparing the marginal value of each element against  $OPT$ . For example, if each element added to a solution with final size  $k$  has a marginal value of at least  $OPT/k$ , then the produced solution would be optimal. Using  $OPT/k$  as a threshold is not practical in most cases, but the central contribution of [8] is to develop a threshold which yields a provably near-optimal solution. The threshold proposed by [8] is

$$T(x|S) = \frac{OPT/2 - f(S)}{k - |S|}. \quad (3)$$

In most cases,  $OPT$  cannot be known *a priori*, so multiple solutions are maintained where each solution has a guess,  $v$ ,

---

#### Algorithm 1 Sieve-Streaming Known Solution Bounds [8]

---

**Given:**  $E, OPT, \overline{OPT}, k$

**Output:**  $\arg \max_{S_v} f(S_v)$

```

1: // Create OPT guesses and solution sets
2:  $O = \{(1 + \epsilon)^i \mid i \in \mathbb{Z}, OPT \leq (1 + \epsilon)^i \leq \overline{OPT}\}$ 
3: for  $v \in O$  do
4:    $S_v \leftarrow \emptyset$ 
5: end for
6: // Make single pass over the input set
7: for  $i \in \{1, 2, \dots, |E|\}$  do
8:   // Find marginal values on parallel threads
9:   for  $v \in O$  do
10:    if  $f(e_i|S_v) \geq \frac{v/2 - f(S_v)}{k - |S_v|}$  &  $|S_v| \leq k$  then
11:       $S_v = S_v \cup e_i$ 
12:    end if
13:   end for
14: end for
```

---

between *a priori* optimal solution bounds  $\overline{OPT} \geq v \geq OPT$ . In the case where multiple solutions are updated throughout the stream,  $OPT$  in (3) is replaced with  $v$ .

**Proposition 1.** (*Sieve-Streaming Solution Bounds [8]*) Given a submodular function  $f$  and known optimal solution bounds, Algorithm 1 satisfies the following properties

- It outputs a solution  $S$  such that  $|S| \leq k$  and  $f(S) \geq (\frac{1}{2} - \epsilon) * OPT$ .
- It does 1 pass over the input set  $E$ , stores at most  $O(\frac{k \log k}{\epsilon})$  elements and has  $O(\frac{\log k}{\epsilon})$  update time per element.

*Proof.* Proposition 1 is a sub-case of Proposition 5.2 from [8] with *a priori*  $OPT$  bounds.  $\square$

Note that the for loop on lines 9-13 of Algorithm 1 evaluates the marginal value of each element with respect to all solutions. This step can be conducted in parallel to dramatically improve computation times. Also note that the suboptimality bound in Proposition 1 does not require the evaluation of all elements, i.e. if all solutions reach the cardinality constraint the algorithm may terminate early.

*Notation:* We denote the input set for geometric map distillation as  $E$ , and the solution set as  $S$ . We assume geometric datasets are collected sequentially as part of a mapping session, and the input set has an indexing function where  $e_i$  denotes the  $i^{th}$  packet of geometric data received in the session. Elements of the input set are point cloud descriptors, where we generate descriptors during an initial dataset processing stream (e.g., during SLAM) using a customized version of [2]. Our descriptors are unit-length 256-dimension vectors that lie on the 255-hypersphere denoted as  $S^{255}$ . When appropriate, we use  $\phi : \mathcal{P} \rightarrow S^{255}$  to describe the descriptor generation function which maps a point cloud onto descriptor space. We use the notation  $d(e, S)$  to denote the minimum Euclidean distance from element  $e$  to set  $S$  such that  $d(e, S) = \min_{v \in S} \|e - v\|_2$ .



#### IV. OPTIMAL GEOMETRIC MAP DISTILLATION

Geometric map distillation is a combinatorial optimization problem which can be formulated as

$$\max_{S \subseteq E, |S| \leq k} f(S), \quad (4)$$

where the input set  $E$  is a set of sequentially collected LiDAR scans. It is assumed that a real-time optimization of (4) has random access to the set of descriptors instead of the point clouds for each element of  $E$  due to computer memory constraints. The remainder of this section will define a function for geometric map *informativeness*, i.e.,  $f(S)$  in (4), which generates representative and diverse solutions when optimized. “Representative” and “diverse” are terms borrowed from [34], where representative solutions in the context of geometric map distillation are those that capture the most unique geometric information, and diverse solutions are those that capture as many different environments from the input set as possible. Additionally, in order to produce distilled maps quickly for real-time autonomy operations, the function should be efficient to evaluate and submodular such that provably near-optimal solutions can be efficiently generated.

The first step in formulating informativeness is to define mutual information—or the measure of redundant information between combinatorial sets—for sets of point clouds. Using the defined mutual information metric, two submodular function classes for map distillation are defined: coverage functions which minimize the mutual information between elements of the solution, and clustering functions which maximize the mutual information between the solution and input sets. We argue that clustering functions are better suited to geometric map distillation and develop a novel submodular clustering function called Continuous Exemplar-Based Clustering. In addition to selecting both representative and diverse solutions, this function can be optimized using a reduced input set which omits sequentially redundant scans with minimal solution quality impact. Optimizing over the reduced input set requires less computation time as the complexity of evaluating any clustering function primarily scales with input set size.

##### A. Point Cloud Mutual Information

A natural metric for defining the mutual information of any two point clouds  $\mathcal{P}_A$  and  $\mathcal{P}_B$  is overlap, formally stated as the intersection over union

$$\mathcal{J}(\mathcal{P}_A, \mathcal{P}_B) = \frac{|\mathcal{P}_A \cap \mathcal{P}_B|}{|\mathcal{P}_A \cup \mathcal{P}_B|}, \quad (5)$$

where the intersection of two point clouds is defined as the set of all points with close points from the other cloud  $\mathcal{P}_A \cap \mathcal{P}_B := \{p \in \mathcal{P}_A | d(p, \mathcal{P}_B) \leq \tau\} \cup \{p \in \mathcal{P}_B | d(p, \mathcal{P}_A) \leq \tau\}$ . The overlap between the solution and the input sets captures the degree of representativeness of a given solution. However, directly maximizing for overlap is computationally expensive, so reward functions that are easy to evaluate and measure (directly or indirectly) overlap are desired.

Learned descriptors can be trained to encode overlap using simple vector operations [2]. The Euclidean distance between descriptors can be used to define point cloud similarity as

$$\mathcal{I}(\mathcal{P}_A, \mathcal{P}_B) = \|\phi(\mathcal{P}_A) - \phi(\mathcal{P}_B)\|_2. \quad (6)$$

The descriptor neural network is trained so that two point clouds with more overlap will have less distance between the corresponding descriptors, so  $\mathcal{I}(\cdot) \approx 1 - \mathcal{J}(\cdot)$ . The limitation of using (6) is that descriptors can only be generated for individual scans. Thus, reward functions designed to assess the informativeness of sets of scans must be developed.

##### B. Submodular Map Coverage vs. Clustering

We identify two possible function classes for geometric map distillation using learned descriptors as a measure of scan-to-scan mutual information. We refer to these function classes as coverage and clustering, which are most similar to other metrics which attempt to capture solution representativeness and diversity in previous submodular summarization work [34]. The goal of this subsection is to provide elementary coverage and clustering functions, prove their submodularity, describe the intuition and differences for each, and ultimately decide which class of functions best captures the desired qualities of informativeness for geometric map distillation.

Coverage functions minimize the mutual information between solution set elements. To define a simple coverage function using descriptors we formulate an area coverage problem over  $\mathcal{S}^{255}$ . Consider each descriptor as the center of a hyperspherical cap with constant radius<sup>2</sup>. We define this coverage function as the area of the union of the caps

$$f(S) = \mathcal{A}(\cup_{s_i \in S} \text{Cap}(s_i)), \quad (7)$$

where  $\mathcal{A}$  is the surface area of the region. Note that coverage encourages diverse solutions because high marginal value elements are those which are distant from other elements of the solution. For this reason, the complexity of computing the marginal value of an element only depends on the size of the current solution. The primary advantage of coverage functions is that evaluation complexity only scales with the size of the solution set which is often much smaller than the input set. Proving that (7) is monotone non-decreasing submodular is similar to many other submodular area coverage functions (e.g., [48] Proposition 2).

Clustering functions maximize the mutual information between the solution and input sets. To define a simple clustering function using descriptors we use the k-mediod loss [56]

$$L(S) = \frac{1}{|E|} \sum_{i=1}^{|E|} d(e_i, S), \quad (8)$$

to define the exemplar-based clustering function

$$f(S) = L(e_0) - L(S \cup e_0). \quad (9)$$

Exemplar-based clustering is proven monotone non-decreasing, submodular in [56] given an appropriate

<sup>2</sup>A hyperspherical cap is the set of points on the surface of a hypersphere which are all within a fixed distance from the center of the cap [55].

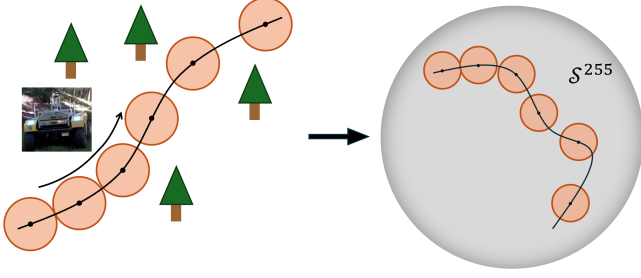


Fig. 3: The descriptors of LiDAR point clouds collected along a time-parameterized trajectory are assumed to be samples along a corresponding trajectory in  $\mathcal{S}^{255}$ . Point clouds and therefore descriptors are assumed to be sampled with unequal distances.

null element  $e_0$ . The origin of the hypersphere  $e_0 = [0, 0, \dots, 0] \in \mathbb{R}^{256}$  can be used in this case as it is a uniform distance of 1 from all points on the sphere, so  $L(e_0) = 1$  and  $f(\emptyset) = 0$ . Clustering functions identify both representative and diverse solution elements because an element must be both distinct from other solution elements and similar to elements of the input set in order to have a high marginal value. However, this means evaluation complexity for clustering functions scales with the size of the input set and is more expensive than coverage functions.

Despite the expected difference in evaluation times, we argue that clustering functions are better suited for geometric map distillation because they reward both representativeness and diversity. In addition to rewarding both these properties, clustering functions also provide more robustness towards outliers and noisy descriptor generation which can be desirable due to the time required to train robust descriptor neural networks and their inability to accurately encode unstructured environments [57]. The primary disadvantage of clustering functions is that the evaluation time scales with the size of the input set. However we can derive a novel clustering function to mitigate this as described in the following subsection.

### C. Continuous Exemplar-Based Clustering

Exemplar-based clustering (9) aims to minimize the average distance between all elements of the input set and the nearest element of the solution set. Because a LiDAR sensor collects scans at a regular frequency and moves with a variable speed, LiDAR datasets often contain arbitrary clusters of repeated scans that result in undesirable bias and computation time when optimizing exemplar-based clustering. For example, if 50% of the scans in a session are taken before the sensor has moved, half of the total score of exemplar-based clustering will be taken from the first repeated sample point. Thus, the effective weight of the first scan will be exaggerated and the resulting solutions will be heavily biased towards including multiple elements near the repeated scans.

To address this bias and reduction computation time, we develop a novel variant called Continuous Exemplar-Based Clustering (CEBC) which finds the unbiased clustering solution for a continuous trajectory with uneven sample frequency. The motivation for CEBC is that geometric perception data is unique for a given pose, so LiDAR scans and the corresponding descriptors can be treated as discrete samples from a con-

tinuous trajectory. Integrating along this trajectory should be a more accurate measure of the breadth of information captured in a mapping session, because sequentially similar samples will contribute less to the overall reward function value. The notion that descriptors are discrete samples from a continuous trajectory is formalized by the following assumption.

**Assumption 1.** Point cloud descriptors are assumed to be discrete samples from a time-parameterized trajectory which we notate as  $\phi(t) : \mathbb{R} \rightarrow \mathcal{S}^{255}$ ,  $t_0 \leq t \leq t_1$ . The trajectory abuses notation for descriptor generation as we assume that each timestamp is associated with a pose and corresponding point cloud which is unique for the geometry of the environment at that pose. Further, we assume sequentially collected descriptors are close to each other such that  $\|e_i - e_{i-1}\|_2 \leq \sigma$  for all  $i$  where  $2 \leq i \leq |E|$ .

Note that for a LiDAR sensor which collects scans at 20 Hz, the descriptor for scan  $e_i$  is identical to the descriptor for the point along this trajectory from the corresponding time, so  $\phi(e_i) = \phi(t_0 + i/20)$ . The CEBC loss term is then formulated as an integral over this trajectory

$$L_{cebc}(S) = \frac{1}{t_1 - t_0} \int_{t_0}^{t_1} d(\phi(t), S) dt. \quad (10)$$

Equation (10) can be transformed into a submodular function similarly to exemplar-based clustering using an appropriate null element. This results in the formal definition of CEBC

$$\Gamma(S) = L_{cebc}(e_0) - L_{cebc}(S \cup e_0), \quad (11)$$

where  $e_0 = [0, 0, \dots] \in \mathbb{R}^{256}$  is the origin again. Similar to (9), because the origin is a unit distance from all points on  $\mathcal{S}^{255}$ ,  $L_{cebc}(e_0) = 1$  and  $\Gamma(\emptyset) = 0$ .

**Proposition 2.** The set function  $\Gamma : 2^E \rightarrow \mathbb{R}$  given in (11) is a monotone non-decreasing, submodular function.

*Proof.* The loss term (10) is monotone non-increasing because of the min operator. Equation (11) is therefore monotone non-decreasing because the first term is constant and the second term is the negative of a monotone non-increasing function.

For (11) to be submodular, it must follow Definition 2 which states that for any two sets  $A \subseteq B \subseteq E$  and element  $e \in E/B$ , we must have  $\Gamma(e|A) \geq \Gamma(e|B) \implies L_{cebc}(A \cup e_0) - L_{cebc}(e \cup A \cup e_0) \geq L_{cebc}(B \cup e_0) - L_{cebc}(e \cup B \cup e_0)$ . Expanding using (10) yields,

$$\begin{aligned} & \int_{t_0}^{t_1} (d(\phi(t), A \cup e_0) - d(\phi(t), A \cup e_0 \cup e)) dt \\ & \geq \int_{t_0}^{t_1} (d(\phi(t), B \cup e_0) - d(\phi(t), B \cup e_0 \cup e)) dt, \end{aligned}$$

where the inequality is true if the integrands follow the inequality for all values of  $\phi(t)$ . The critical step in establishing the above inequality is that the min operator is monotone non-increasing, meaning that minimizing a function over one set will yield a value greater than or equal to that obtained by minimizing the same function over a larger input set. We can prove the integrands follow the inequality by considering two possible scenarios where  $\phi(t)$  is either closer to  $x$  or  $B \cup e_0$ .

If  $d(\phi(t), e) \leq d(\phi(t), B \cup e_0)$ , then we have  $d(\phi(t), e) \leq d(\phi(t), A \cup e_0)$  because every element in  $B \cup e_0$  is also an element in  $A \cup e_0$  and

$$\begin{aligned} d(\phi(t), A \cup e_0) - d(\phi(t), e) &\geq d(\phi(t), B \cup e_0) - d(\phi(t), e) \\ \implies d(\phi(t), A \cup e_0) &\geq d(\phi(t), B \cup e_0), \end{aligned}$$

which must be true because the min operator is monotone non-increasing and the first term is minimized over a smaller set  $A \cup e_0 \subseteq B \cup e_0$ . If instead  $d(\phi(t), e) > d(\phi(t), B \cup e_0)$  then the right-hand side cancels out and we have,  $d(\phi(t), A \cup e_0) - d(\phi(t), A \cup e_0 \cup e) \geq 0$ , which must be true because the min operator is monotone non-increasing and the first term is again minimized over a smaller set  $A \cup e_0 \subseteq e \cup A \cup e_0$ . Hence, we have shown the integrands follow the inequality, so (11) is a monotone non-decreasing, submodular function.  $\square$

Although (11) theoretically addresses the problem of over-sampling arbitrary locations in input LiDAR sets, the integral in (10) is impossible to evaluate because we do not have access to  $\phi(t)$  as a continuous function. Instead, we use a discrete approximation of a path integral with a weighted sum of all the sample points

$$L_{disc}(S) = \frac{1}{d_{tot}} \sum_{i=2}^{|E|} w_i d(e_i, S), \quad (12)$$

where  $d_{tot}$  is the total path length and  $w_i$  is the weight for element  $e_i$ . The discrete approximation of a path integral requires weighting each sample point by the path length to neighboring sample points<sup>3</sup>. We can approximate this element weighting using the distance between sequential elements so that  $w_i = \|e_i - e_{i-1}\|_2$ . The total path length is then approximated as  $d_{tot} = \sum w_i$ .

A desired property of (11) is that sequentially similar elements (e.g. LiDAR scans taken from the same position) will have very low weights and can be ignored with minimal impact. Therefore, the goal of the remainder of this section will be to show that the value of CEBC does not change much when evaluated using a full or reduced set, and that any solution composed of elements from the full set has a close solution composed of elements from the reduced set.

Algorithm 2 gives our method for selecting a reduced input set (denoted as  $R$ ) with individual elements  $r_i$ . The elements of the reduced set are selected such that they all have at least  $\mathcal{E}$  path length between them if  $\mathcal{E} \geq \sigma$ . We assume that when building a reduced input set, an injective mapping function  $\theta : \mathbb{Z} \rightarrow \mathbb{Z}$  is saved which translates indices from the reduced set to the corresponding index in the full set such that  $r_i = e_{\theta(i)}$ . When optimizing (11) with the reduced set, element weights are assigned as a sum over the distances between elements of the full input set such that  $\hat{w}_i = \sum_{j=\theta(i-1)+1}^{\theta(i)} w_j$  (lines 3, 6, & 10). Because we assume sequential descriptors are no further than  $\sigma$  apart and  $\mathcal{E} \geq \sigma$ , the max reduced set weight is bounded by  $\hat{w}_i \leq 2\mathcal{E}$ . The total distance  $d_{tot}$  is calculated the same way and therefore remains constant.

<sup>3</sup>There are many methods for discretely approximating continuous integrals, here we rely on a simple first-order method.

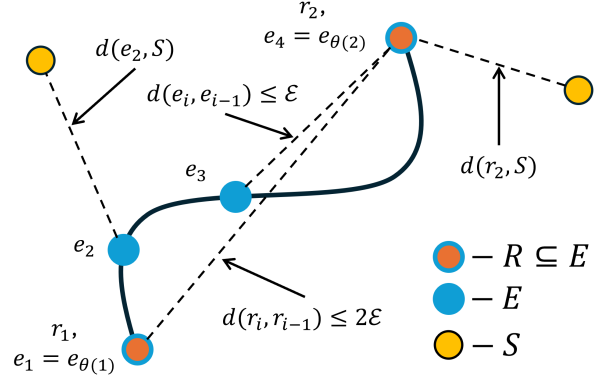


Fig. 4: Section of a full and reduced set generated by Algorithm 2. All elements in the full set (blue outlines) are no further than  $\mathcal{E}$  apart, and all elements of the reduced set (orange interior) are no further than  $2\mathcal{E}$  apart. The weight assigned to  $r_2$  is the sum of weights from its source set  $\hat{w}_2 = w_2 + w_3 + w_4$ . The closest element of  $S$  to  $e_2$  and  $r_2$  does not have to be the same element of the solution  $S$ .

#### Algorithm 2 Reduced Input Set Selection

**Given:**  $E, \mathcal{E} > 0$

**Output:**  $R$

```

1:  $R = \{e_1\}, \hat{W} = \{0\}, w = 0$ 
2: for  $i = \{2, 3, \dots, |E|\}$  do
3:    $w = w + \|e_i - e_{i-1}\|_2$ 
4:   if  $w \geq \mathcal{E}$  then
5:      $R = R \cup \{e_i\}$ 
6:      $\hat{W} = \hat{W} \cup \{w\}$ 
7:   end if
8: end for
9:  $R = R \cup \{e_{|E|}\}$ 
10:  $\hat{W} = \hat{W} \cup \{w\}$ 
```

We define the set of elements  $\{e_j | j \in [\theta(i-1) + 1, \theta(i) - 1] + 2, \dots, \theta(i)\}$  as the source set for  $r_i$  because the weight for  $r_i$  in the reduced set is the sum of weights from the source set. It will be convenient to denote the set of indices in the source set as  $\eta_i = [\theta(i-1) + 1, \theta(i-1) + 2, \dots, \theta(i)]$ . In the following lemma, we prove the minimum distance from an element of the reduced set to an arbitrary solution  $S$  and the elements of its source set to  $S$  is similar.

**Lemma 1.** Consider an input set of elements  $E$  and corresponding reduced set  $R$  built using Algorithm 2 with  $\mathcal{E} \geq \sigma$ . For any element  $r_i$  and any element from the corresponding source set  $e_j, j \in \eta_i$ , then  $|d(r_i, S) - d(e_j, S)| \leq 2\mathcal{E}$ .

*Proof.* The distance between  $r_i$  and its source set is bounded by  $d(r_i, e_j) \leq 2\mathcal{E}, \forall j \in \eta_i$ . Consider the elements in  $S$  closest to  $r_i$  and  $e_j$  and denote them as  $v$  and  $u$  respectively. Note that  $v$  and  $u$  do not need to be the same element as shown in Fig. 4. Then the distance from  $r_i$  to  $S$  can be related to  $e_j$  by  $d(r_i, v) \leq d(r_i, u) \leq d(r_i, e_j) + d(e_j, u) \leq 2\mathcal{E} + d(e_j, u)$ . This simplifies to  $d(r_i, v) \leq d(e_j, u) + 2\mathcal{E}$ , which can be manipulated into  $|d(r_i, S) - d(e_j, S)| \leq 2\mathcal{E}$ .  $\square$

In the following proposition, we prove that the value of a solution is arbitrarily similar for (11) when using  $E$  and  $R$ .



**Proposition 3.** Consider an input set of elements  $E$  and corresponding reduced set  $R$  built using Algorithm 2 with  $\mathcal{E} \geq \sigma$ . Also consider the submodular function  $\Gamma_E(S) = L_{disc}(e_0) - L_{disc}(S \cup e_0)$  which indicates the input set (either  $E$  or  $R$ ) by the subscript. For any solution  $S$ ,  $|\Gamma_E(S) - \Gamma_R(S)| \leq 2\mathcal{E}$ .

*Proof.* The proof follows from Lemma 1 as the value of each source set can be associated with the corresponding element of the reduced set. Using (12), we have

$$|\Gamma_E(S) - \Gamma_R(S)| = \frac{1}{d_{tot}} \left| \sum_{i=1}^{|E|} w_i d(e_i, S) - \sum_{i=1}^{|R|} \hat{w}_i d(r_i, S) \right|.$$

Splitting the sum over the full set into sums over reduced set elements,

$$|\Gamma_E(S) - \Gamma_R(S)| = \frac{1}{d_{tot}} \sum_{i=1}^{|R|} \left| \sum_{j \in \eta_i} w_j d(e_j, S) - \hat{w}_i d(r_i, S) \right|$$

Factoring out  $\hat{w}_i = \sum_{j \in \eta_i} w_j$ ,

$$|\Gamma_E(S) - \Gamma_R(S)| = \frac{1}{d_{tot}} \sum_{i=1}^{|R|} \left| \sum_{j \in \eta_i} w_j (d(e_j, S) - d(r_i, S)) \right|.$$

Finally, applying Lemma 1, we get the desired inequality

$$\begin{aligned} |\Gamma_E(S) - \Gamma_R(S)| &\leq \frac{1}{d_{tot}} \sum_{i=1}^{|R|} \left| \sum_{j \in \eta_i} 2w_j \mathcal{E} \right| \\ &= \frac{2\mathcal{E}}{d_{tot}} \sum_{i=1}^{|R|} \hat{w}_i \\ &= 2\mathcal{E}. \end{aligned} \quad \square$$

Proposition 3 proves that for any arbitrary solution, the value of (11) evaluated on the full or reduced set is similar. Next, we show that any solution composed of elements from the full set,  $S_E$ , has a similar solution composed of elements from the reduced set,  $S_R$ . By Algorithm 2, any element of the full set has a corresponding element of the reduced set no further than  $\mathcal{E}$  away. This means the elements of solution  $S_E$  can each be shifted by up to  $\mathcal{E}$  in order to find a corresponding solution  $S_R$ . In order to bound the total loss caused by this shift, we conservatively assume that all elements had their closest corresponding solution element moved the maximum distance away. This results in a tight bound for the shifted solution value based on the original solution  $\Gamma(S_R) = L_{disc}(e_0) - L_{disc}(S_R \cup e_0) \geq 1 - \frac{1}{d_{tot}} \sum_{i=2}^{|E|} w_i (d(e_i, S_E \cup e_0) + \mathcal{E}) = \Gamma(S_E) - \mathcal{E}$ . Simplifying the above, the desired inequality  $\Gamma(S_R) \geq \Gamma(S_E) - \mathcal{E}$  is achieved which states that any solution composed of elements from  $E$  has an arbitrarily similar solution composed of elements from  $R$ .

Continuous exemplar-based clustering is well suited as a reward function for geometric map distillation because it selects the solution which best represents the input set. CEBC is evaluated efficiently and avoids bias towards over-sampled positions because of the ability to remove sequentially redundant elements with minimal loss. Importantly, CEBC is submodular, meaning efficient algorithms for maximizing it with provably tight suboptimality guarantees exist.

## V. DYNAMICALLY REORDERED STREAMING SUBMODULAR MAXIMIZATION

Optimizing CEBC (11) for geometric map distillation is computationally challenging because input sets frequently contain tens of thousands of scans. Equation (11) is submodular though, meaning multiple algorithms with polynomial-complexity are available to generate provably near-optimal solutions. Streaming submodular maximization algorithms are well-suited for optimizing over large input datasets because they only require a single pass over the input set. This is in contrast to the more popular greedy algorithm which requires  $k$  passes to generate a solution of size  $k$ . The downside of streaming is that elements are evaluated before the entire input set has been processed, so the algorithm must build solutions with limited information. One such consequence of limited information is input order bias, or the increased likelihood of selecting elements due to the order of the stream.

This section presents a streaming submodular algorithm for geometric map distillation which efficiently addresses input order bias. This is accomplished by using approximate marginal values of unchecked elements to dynamically reorder the stream such that the next element always has high expected value. We begin by defining two forms of input order bias which degrade streaming algorithm performance relative to the greedy algorithm. The dynamically reordered streaming submodular algorithm is then presented under the assumption that a suitable marginal value approximation function for CEBC exists. We conclude the section by defining two functions for approximating the marginal value of (11) which require  $O(1)$  computations to evaluate.

### A. Input Order Bias in Streaming Submodular Maximization

Input order bias is defined for streaming submodular maximization as the increased likelihood of solutions containing elements solely due to their position in the stream of the input set. Bias is introduced to streaming algorithms because of the need to make decisions on including elements before evaluating the entire stream, i.e., using limited information. We identify two forms of input order bias which we refer to as opportunity cost and threshold saturation bias.

**Opportunity Cost Bias:** A naive approach to streaming submodular maximization would be to only admit elements with a marginal value of at least  $OPT/k$ . If this approach managed to admit  $k$  elements it is easy to show that the generated solution must be optimal, but [8] proves that such an approach fails for trivial scenarios. Streaming algorithms must therefore rely on relaxed thresholds that admit suboptimal elements (e.g., (3)) to achieve a near  $1/2$ -suboptimality bound. This means that given two elements with similar value, the one seen earlier is more likely to be included in the generated solution because (i) the solution might be full by the time it reaches the second element, or (ii) the mutual information of the first might lower the marginal value of the second element.

Opportunity cost bias is thus defined as the increased likelihood of streaming submodular algorithms to select elements that appear earlier in the stream due to relaxed admission thresholds. The loss of efficiency for streaming submodular

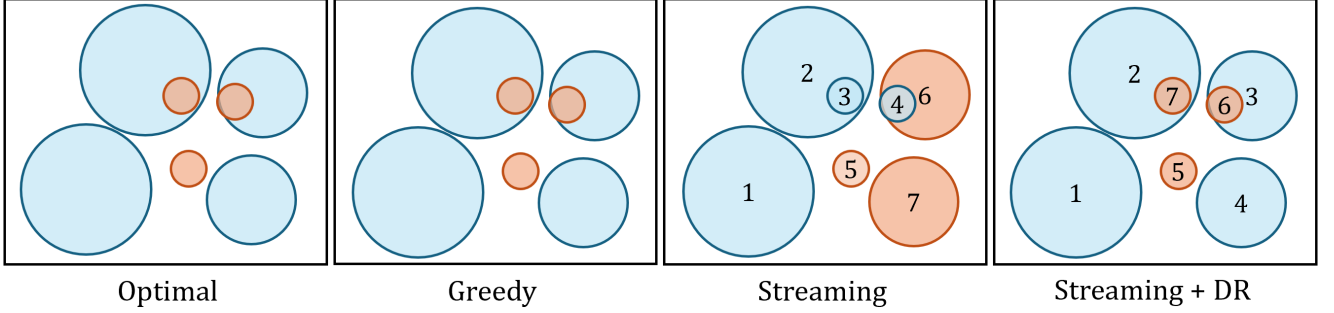


Fig. 5: Sensor coverage selection problem with a maximum limit of four selected sensors. Sensors in the solution set are blue, and sensors not included in the solution are orange. From left to right: optimal solution, solution generated by the greedy algorithm which does not consider input order, streaming solution with the input order indicated by the numbers in the middle of the sensor footprints, and the streaming solution with dynamic reordering (DR) which modifies the input order according to approximate element values. Assumed that  $OPT$  is known *a priori* and only one solution is maintained by the streaming variants.

maximization relative to the greedy algorithm due to opportunity cost bias is demonstrated in Fig. 5. In the third pane, the default streaming algorithm adopts an arbitrary stream order indicated by the numbers in the sensor footprints. Although the 6th sensor in the stream covers more area than the 4th, it is not adopted in part because the 4th was considered earlier.

**Threshold Saturation Bias:** The relaxed admission threshold introduces another form of input order bias as it adjusts to the value of the current solution. Recall that streaming submodular algorithms maintain multiple solutions in parallel, each with their own guess of the optimal solution value  $v$ . When a solution value exceeds  $v/2$ , the admission threshold given by (3) becomes negative, meaning that any evaluated element will be added to the solution after this point until the solution reaches the cardinality constraint.

Threshold saturation bias is thus defined as the bias towards elements in the stream evaluated immediately after a solution value reaches  $v/2$ . Although it would be impossible to know when a solution reaches a value of  $v/2$ , several conditions present in geometric map distillation mean this threshold is regularly reached early in the stream. Notably, most elements have a similar value, meaning the average value of any one element alone is close to  $OPT/k$ . Thus the first  $k/2$  elements with low mutual information will likely be adopted, with the remaining  $k/2$  elements adopted regardless of their marginal value. Threshold saturation bias is demonstrated in Fig. 5 where the solution generated by the streaming algorithm exceeds a value of  $OPT/2$  after including just the first two elements. Once saturated, the remainder of the solution is determined entirely by stream order and the 3rd sensor is chosen despite having zero marginal value.

### B. Streaming Submodular Dynamic Reordering

We propose dynamic reordering as our solution to input order bias in streaming submodular maximization for geometric map distillation. The goal of dynamic reordering is to actively select stream order such that elements with high expected value are presented earlier and are therefore more likely to be included in solutions as a result of input order bias. Expected marginal values – those obtained from an approximation of CEBC or heuristic denoted with  $\hat{\Gamma}$  – must be used because complete knowledge of the marginal value of each element would require evaluating the entire input set at least  $k$  times,

reducing it to a classical greedy approach. Because each element may have a different marginal value with respect to each solution, *ordering scores* are generated by taking the average expected marginal value for an element across all solutions. Deciding which element to present next at each step in the stream introduces additional computational burden, but this can be mitigated by limiting the set of elements which can be searched over at each step. The remainder of this section describes the process of dynamic reordering in greater detail.

The dynamically reordered streaming submodular algorithm for geometric map distillation is given by Algorithm 3. Intuitively, Algorithm 3 closely mirrors Sieve-Streaming (Algorithm 1) with additional steps for efficiently tracking and updating the score of CEBC and the ordering scores used to select stream order. Multiple solutions are initialized on lines 2-5 identically to Sieve-Streaming. Lines 7-8 include the first deviation, where a sorted and unsorted set are initialized. We note that the input set order is randomized before optimization, and that both the sorted and unsorted sets are assumed to have mapping functions which relate the index of the order score to the element in  $E$  such that  $e_i$  has order score  $\Theta_S(\gamma(i))$  if it is in the sorted set or  $\Theta_U(\kappa(i))$  if it is in the unsorted set. The goal of the sorted set is to minimize the computational burden of dynamic reordering by limiting the available elements to evaluate next in the stream to a fixed size set. The size of the sorted set is controlled by the parameter  $F$  as the sorted set will always have no more than  $Fk$  elements. The single evaluation pass occurs on lines 10-16, where the details of key functions are left to their own algorithm blocks.

The selection process for deciding which element to evaluate next is given by Algorithm 4. This simple function returns the index of the highest scored element of the sorted set after removing that element and refilling the sorted set. This function illuminates the purpose of the sorted set: where finding the next index from a complete set requires an  $O(|E|\log|E|)$  complexity search for the highest valued element, keeping a sorted set reduces the complexity to  $O(Fk * \log(Fk))$  which can be directly controlled by the parameter  $F$ .

The process for evaluating elements and updating ordering scores is described in Algorithm 5. The algorithm begins by making a copy of the sorted and unsorted sets (line 1) which will be saved if the element is included in the solution. The marginal value  $\Gamma(e_i|S_v)$  of the element is found incrementally

---

**Algorithm 3** Dynamically Reordered (DR) Streaming Submodular Maximization

---

**Given:**  $E, \underline{OPT}, \overline{OPT}, k, F$ 
**Output:**  $\arg \max_{S_v} f(S_v)$ 

```

1: // Create OPT guesses and solution sets
2:  $O = \{(1 + \epsilon)^i | i \in \mathbb{Z}, \underline{OPT} \leq (1 + \epsilon)^i \leq \overline{OPT}\}$ 
3: for  $v \in \{1, 2, \dots, |O|\}$  do
4:    $S_v = \emptyset$ 
5: end for
6: // Create partitions of indices and order scores
7:  $\Theta_S \leftarrow \text{ones}(F * k)$ 
8:  $\Theta_U \leftarrow \text{ones}(|E| - F * k)$ 
9: // Make single pass over the input set
10: for  $a \in \{1, 2, \dots, |E|\}$  do
11:    $i = \text{NextIndex}(\Theta_S, \Theta_U)$ 
12:   // Parallel evaluation step over all solutions
13:   for  $v \in \{1, 2, \dots, |O|\}$  do
14:      $\text{ElementEvaluation}(i, E, \Theta_S, \Theta_U, S_v)$ 
15:   end for
16: end for
```

---



---

**Algorithm 4** Next Index

---

**Given:**  $\Theta_S, \Theta_U$ 
**Output:**  $i$ 

```

1:  $i = \gamma^{-1}(\arg \max_j \Theta_S(j))$ 
2:  $\Theta_S.\text{remove}(\gamma(i))$ 
3:  $\Theta_S.\text{append}(\Theta_U(0))$ 
4:  $\Theta_U.\text{remove}(0)$ 
```

---

during the evaluation pass (lines 3-13) and initialized on line 2. The marginal value of  $e_i$  is determined by finding the elements of the input set such that  $d(e_i, e_j) < d(e_j, S)$ . If an input set element is closer to  $e_i$  than the current solution (lines 4-5), then the marginal value score is increased by the difference in the distances weighted by the input set element's weighting. On lines 7-11, the ordering score is updated by taking the difference in  $\hat{\Gamma}$  divided by the number of solutions such that the average value is maintained (lines 8 and 10).  $\hat{\Gamma}$  is assumed monotone-increasing such that when  $d < d(e_i, S_v)$ ,  $\hat{\Gamma}(d) < \hat{\Gamma}(d(e_i, S_v))$ . This means that lines 8 and 10 decrease the ordering score because this new element has a higher degree of mutual information with it.

### C. Approximating CEBC for Dynamic Reordering

Central to the efficiency of dynamic reordering is an efficient method for approximating the relative marginal value of an element with respect to any solution, given as  $\hat{\Gamma}(e_i|S_v)$  in Algorithm 5. We note that the approximation functions only need to recover the relative marginal values such that  $\hat{\Gamma}(e_i|S_v) > \hat{\Gamma}(e_j|S_v)$  if  $\Gamma(e_i|S_v) > \Gamma(e_j|S_v)$ . This is because dynamic reordering only uses ordering scores to select the next element of the stream. In this subsection, a heuristic function and approximation of (11) are derived which can be used as  $\hat{\Gamma}$ , with the commonality between both approaches being the efficient,  $O(1)$  evaluation complexity. Both approaches

---

**Algorithm 5** Element Evaluation

---

**Given:**  $i, E, \Theta_S, \Theta_U, S_v$ 

```

1:  $\Theta_{S,n} = \Theta_S, \Theta_{U,n} = \Theta_U$ 
2:  $\Gamma(e_i|S_v) = 0$ 
3: for  $j \in \{1, 2, \dots, |E|\}$  do
4:    $d = \|e_i - e_j\|_2$ 
5:   if  $d < d(e_j, S_v)$  then
6:      $\Gamma(e_i|S_v) + = \frac{w_j}{d_{tot}}(d(e_j, S_v) - d)$ 
7:     if  $j \leq |\Theta_S|$  then
8:        $\Theta_{S,n}(\gamma(j)) + = \frac{1}{|\Theta|}(\hat{\Gamma}(d) - \hat{\Gamma}(d(e_j, S_v)))$ 
9:     else if  $j \leq |\Theta_U|$  then
10:       $\Theta_{U,n}(\kappa(j)) + = \frac{1}{|\Theta|}(\hat{\Gamma}(d) - \hat{\Gamma}(d(e_j, S_v)))$ 
11:     end if
12:   end if
13: end for
14: if  $\Gamma(e_i|S_v) \geq \frac{v/2 - f(S_v)}{k - |S_v|} \& |S_v| \leq k$  then
15:    $S_v = S_v \cup e_i$ 
16:    $\Theta_S = \Theta_{S,n}, \Theta_U = \Theta_{U,n}$ 
17: end if
```

---

effectively convert (11) into an area coverage problem which is easier to evaluate as described in Section IV-B.

**Heuristic approximation** of  $\Gamma$  can be achieved using the known positions of each scan in the mapping dataset. Given the position of all elements in the solution set as  $X_S = [\mathbf{x}_1, \mathbf{x}_2, \dots, \mathbf{x}_{|S|}]$  where  $\mathbf{x}_i \in \mathbb{R}^3$ , the pose approximate marginal value of an element with pose  $\mathbf{x}_e$  is

$$\hat{\Gamma}(x) = \Gamma_{pose}(d(\mathbf{x}_e, X_S)) = 1 - \max(0, -\log(d(\mathbf{x}_e, X_S)/\alpha + 0.1)), \quad (13)$$

where  $\alpha$  is a tunable radius parameter. Using (13) in Algorithm 5 requires changing the input on lines 8 and 10 from the difference in descriptor distances to the difference in pose distances. The log function introduces a decay which is intended to mimic the overlapping area of 2D sensors with circular footprints. This heuristic can fail when small position differences correspond to large differences in overlap, such as scans taken from either side of a wall.

**CEBC approximation** is achieved by converting (11) into an area coverage function over  $S^{255}$ . The marginal value of this function can be precomputed for solutions with two or fewer elements, meaning pairwise information can be known *a priori* as a single input function of the distance between the two elements of the solution. Pairwise information can then be used to define an optimistic approximate marginal value which can be found with  $O(1)$  computations.

To convert (11) into a coverage function over  $S^{255}$ , we make the assumption that the solution set is selected from  $E$ , but evaluated against every possible point on  $S^{255}$ . By replacing  $E$  with  $S^{255}$  in (10), a coverage loss function is derived

$$L_{cebc} \approx L_{cover}(S) = \frac{1}{\mathcal{A}(S)} \int_S \min_{v \in S} \|v - x\|_2 d\sigma. \quad (14)$$

Note that the superscript denoting the dimension of the hypersphere is omitted for clarity, and  $\mathcal{A}(S)$  is the surface area of the hypersphere. Converting this loss term into a submodular



function is similar to exemplar-based clustering and CEBC

$$f_{\text{cover}}(S) = L_{\text{cover}}(e_0) - L_{\text{cover}}(S \cup e_0), \quad (15)$$

using the origin  $e_0 = [0, 0, \dots, 0] \in \mathbb{R}^{256}$  as the null element.

Although (15) can be evaluated independently of  $E$ , it remains computationally expensive because it requires integrating over the entire surface of a high-dimension hypersphere. Additionally, the fraction of a high-dimension hypersphere covered by a spherical cap is vanishingly small [55], so (14) will equal 1 even for very large solutions. The integration can be simplified and made numerically well-conditioned by separating  $\mathcal{S}^{255}$  into regions based on which element of  $S \cup e_0$  they are closer to. In this way, (14) and (15) can be understood using hyperspherical caps, where elements closer to  $S$  than  $e_0$  are those which are within a distance of 1 from any element of  $S$ . We define the region of  $\mathcal{S}^{255}$  near  $S$  as the union of spherical caps centered at the descriptors in  $S$  with radii of 1, notated as  $\mathcal{C}(S) := \{x \in \mathcal{S}^{255} \mid \|v - x\|_2 \leq 1, \forall v \in S\}$ . We also define the complement of this region as  $\mathcal{C}^-(S) := \{x \in \mathcal{S}^{255} \mid \|v - x\|_2 > 1, \forall v \in S\}$ . Because they are complementing areas of the hypersphere,  $A(S) = A(\mathcal{C}) + A(\mathcal{C}^-)$ .

An equivalent function for maximizing (15) which only integrates over  $\mathcal{C}$  (and is therefore well-conditioned) is

$$\Gamma_C(S) = A(\mathcal{C}) - \int_{\mathcal{C}} d(x, S) d\sigma. \quad (16)$$

We show that (15) achieves maximum value with the optimal solution of (16) in the following proposition.

**Proposition 4.** *The elements that maximize (15) are equivalent to those that maximize (16).*

*Proof.* Note that  $e_0$  is always a unit distance from any surface element of the hypersphere, so when evaluating (14) with only the null element  $L_{\text{cover}}(e_0) = \int_{\mathcal{S}} 1 d\sigma = A(\mathcal{S})$ . We can also evaluate  $L_{\text{cover}}(S \cup e_0)$  as a sum of the integral over  $\mathcal{C}$  and  $\mathcal{C}^-$  where  $L_{\text{cover}}(S \cup e_0) = \int_{\mathcal{C}} \min_{v \in S} \|v - x\|_2 d\sigma + \int_{\mathcal{C}^-} 1 d\sigma$ . By plugging in (14), (15) can be rewritten as

$$f_{\text{cover}}(S) = \frac{1}{A(\mathcal{S})} \left( A(\mathcal{S}) - \int_{\mathcal{S}} d(x, S \cup e_0) d\sigma \right).$$

Integrating  $L_{\text{cover}}(S \cup e_0)$  over  $\mathcal{C}$  and  $\mathcal{C}^-$  separately, we get

$$f_{\text{cover}}(S) = \frac{1}{A(\mathcal{S})} \left( A(\mathcal{S}) - A(\mathcal{C}^-) + \int_{\mathcal{C}} d(x, S) d\sigma \right).$$

Recalling  $A(\mathcal{C}^-) = A(\mathcal{S}) - A(\mathcal{C})$ , then

$$f_{\text{cover}}(S) = \frac{1}{A(\mathcal{S})} \left( A(\mathcal{C}) - \int_{\mathcal{C}} d(x, S) d\sigma \right),$$

which, using (16), simplifies to

$$f_{\text{cover}}(S) = \frac{1}{A(\mathcal{S})} \Gamma_C(S).$$

Taking  $\arg \max$  over  $S$  of both sides yields

$$\arg \max_S f_{\text{cover}}(S) = \arg \max_S \Gamma_C(S)$$

where we have used the property that scaling a cost function by a constant does not change the optimal solution. Hence,

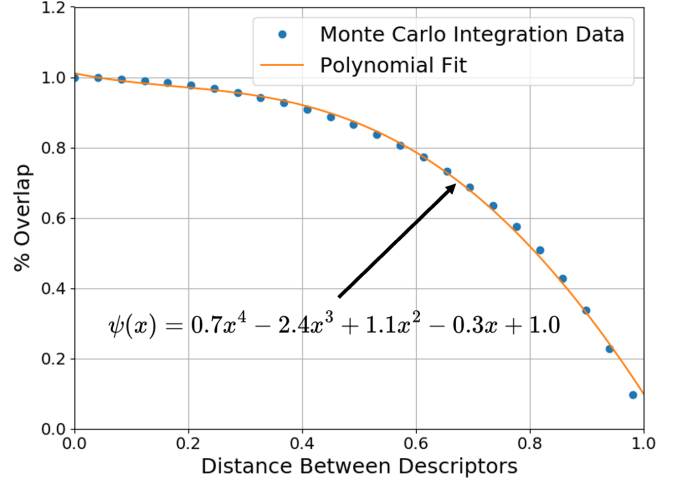


Fig. 6: Mutual information with respect to (16) as percent overlap between spherical caps. Overlap percent is obtained as a function of the distance between descriptors using a dense Monte Carlo integration over the surface of  $\mathcal{S}^{255}$ , with a fourth order polynomial function  $\psi(x)$ .

the elements that maximize (15) also maximize (16).  $\square$

Computing the marginal value of (16) is still difficult, but can be simplified using pairwise information. Note that any solution with one element will have a constant value  $\Gamma_C(S) = c$ . Due to symmetry, the value of any solution with two elements can be reduced to a single input function of the distance between the two elements. We define the degree of mutual information between two elements  $s_1$  and  $s_2$  as  $\mathcal{O}(d(s_1, s_2)) : \mathbb{R} \rightarrow \mathbb{R}$ . Thus, the value of any solution with two elements is  $\Gamma_C(S) = c + c(1 - \mathcal{O}(d(s_1, s_2)))$ . Computing  $\mathcal{O}(d(s_1, s_2))$  can be done offline and approximated using the polynomial given as  $\psi(x)$  in Fig. 6. If spherical caps centers are further than 1.1 apart they have no overlap, so the pairwise mutual information function is defined as

$$\mathcal{O}(d(s_1, s_2)) = \begin{cases} \psi(d(s_1, s_2)) & \text{if } d(s_1, s_2) < 1.1 \\ 0 & \text{otherwise.} \end{cases} \quad (17)$$

The pairwise marginal value approximation of (16) can then serve as an approximation for the marginal value of (11). Specifically, the approximation function  $\hat{\Gamma}(x)$  used for generating order scores in dynamic reordering is

$$\hat{\Gamma}(x) = \bar{\Gamma}_C(d(e, S)) \propto 1 - \mathcal{O}(d(e, S)). \quad (18)$$

When  $\hat{\Gamma}(x)$  is evaluated on lines 8 and 10 of Algorithm 5, the new element is already known to be closer than any element in the solution so  $d(e, S)$  is assumed known when evaluating (18). The single element score constant  $c$  is dropped because only the relative value of ordering scores is required.

Dynamic reordering uses approximate marginal value functions with  $O(1)$  evaluation complexity such as (13) and (18) to actively order the stream such that input order bias favors elements with high expected value. Additional computation and memory costs are introduced by maintaining and sorting the ordering scores. However, this additional burden can be offset by fewer CEBC evaluations if solution sets reach the cardinality constraint earlier in the stream, which can be

**Algorithm 6** Heuristic Solution for Initial Lower Bound**Given:**  $E, k$ **Output:**  $\underline{OPT} \leftarrow f(S_h)$ 


---

```

1:  $d_{tot} = 0$ 
2: for  $i \in \{2, 3, \dots, |E|\}$  do
3:    $d_{tot} = d_{tot} + \|e_i - e_{i-1}\|_2$ 
4: end for
5:  $S_h = \emptyset$ 
6: while  $|S_h| \leq k$  do
7:    $d = 0$ 
8:   while  $d \leq d_{tot}/k$  do
9:      $d = d + \|e_i - e_{i-1}\|_2$ 
10:  end while
11:   $S_h = S_h \cup e_i$ 
12: end while

```

---

expected as more elements will have higher expected marginal value. Additionally, limiting the size of the sorted set via the sorted set factor size limits the additional computational burden of sorting the ordering scores.

## VI. ALGORITHMIC IMPLEMENTATION

This section describes algorithmic innovations which reduce OptMap’s computation time. In the first subsection, we describe the methods used to generate tight initial optimal solution bounds, in the second we describe our process for performing map optimization and loading on parallel threads, and in the final we briefly describe the position and time constraints which can be passed as additional arguments.

## A. Initial Lower Bound

The time complexity of streaming submodular maximization algorithms can vary significantly depending on the existence or quality of *a priori* solution value bounds. This is because tight bounds allow for fewer maintained solutions which ultimately require fewer computations. Algorithm 6 describes our method for generating a heuristic solution which can be used to obtain an initial lower bound. The heuristic solution finds  $k$  elements with equal distance *along the descriptor trajectory*, where the equal spacing works best in mapping datasets which explore new environments at consistent rates. Lines 1-4 are performed alongside the reduced set selection from Algorithm 2, where the total descriptor trajectory length is calculated by summing the total distance between all sequential input set elements. The heuristic solution is thus built (lines 5-12) by selecting elements from the input set at regular intervals of  $d_{tot}/k$ . The lower bound is obtained by evaluating the heuristic solution on (11) which requires one evaluation pass.

The maximum value of (11) is simple to obtain and is achieved when the solution set contains the entire solution set. In this case, the second loss term in (11) equates to 0, and thus the upper bound is always  $\overline{OPT} = 1$ .

## B. Parallel Map Loading and Optimization

OptMap saves point clouds in computer storage after using them to generate descriptors due to computer memory constraints. Loading the distilled maps after optimization then

presents a significant portion of OptMap’s total return time because the saved point clouds are dense and must be loaded in serial on a single processor thread. However, the best incomplete solution may be loaded in many cases before the optimization completes because (i) many solutions contain similar scans, so if a scan is loaded for one solution it may still save load time for another solution, and (ii) the best solution often maintains an equal or higher value than all other solutions throughout the optimization. Both these properties are more likely because tight initial bounds result in fewer solutions which all share similar admission threshold values. Map load times can therefore be reduced by using some of the optimization time to begin preloading the solution. Solutions can begin loading on a separate thread if the same solution maintains the highest score for  $N$  steps of the stream (we set this to 20 by default).

## C. Position and Time Constraints

The input set can be further constrained by applying additional position and time constraints. Position constraints are defined using a set of balls  $(x_c, r)$ , where  $x_c$  is the coordinates of the ball center and  $r$  the radius, and time constraints are defined with a set of initial and final timestamps  $(t_i, t_f)$ . Each element of the input set is a scan with an associated position  $x(e_i)$  and time  $t(e_i)$ . The filtered input set is then the subset of the input set with poses and timestamps inside the defined position and time constraints, defined as  $E_c := \{e_i \in E \mid \|x(e_i) - x_c\|_2 \leq r, t(e_i) \in [t_i, t_f]\}$ . Multiple constraints can be applied, giving OptMap the ability to distill specified portions of a mapping session. An example of the position constraints are shown in Fig. 1a, where position and time constraints are seen as valuable tools for customizing distilled maps to specific downstream applications.

## VII. RESULTS

In this section, we provide results that demonstrate OptMap’s theoretical contributions, expected distilled map quality, and computational performance. The first result compares Continuous Exemplar-Based Clustering (11) to Exemplar-Based Clustering (9), a descriptor coverage function (7), and an optimal but computationally infeasible overlap metric. The second result is an ablation study that compares dynamically reordered streaming submodular maximization using three possible approximation functions to the baseline Sieve-Streaming algorithm, the heuristic method given by Algorithm 6, and random selection. The final result highlights OptMap’s minimal computation requirements and potential applications via multiple large-scale map summarization scenarios. The first two results include custom LiDAR datasets collected on the UCLA campus using 32-beam Ouster OS0 and OS1 sensors, and custom datasets from the Army Research Laboratory Graces Quarters facility collected using a 128-beam Ouster OS1 sensor. The final result uses a long-duration custom dataset from the Army Research Laboratory collected on the same 128-beam Ouster OS1 sensor and five separate mapping sessions from the Oxford Spires [58], Semantic KITTI [59], and Newer College Datasets [60].

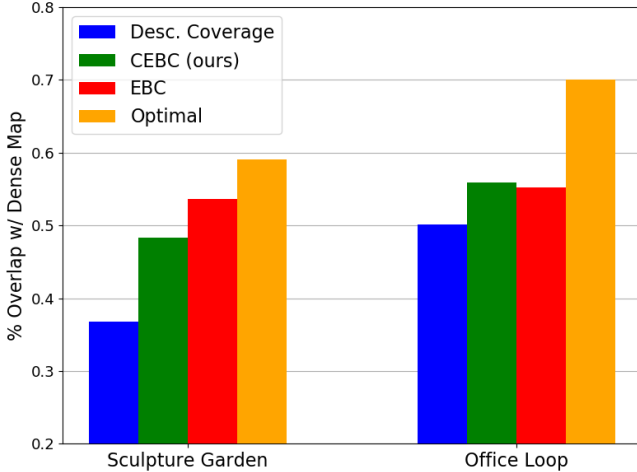


Fig. 7: Percent overlap of distilled maps for reward functions when maximized via the greedy algorithm, higher indicates better performance. EBC slightly outperforms CEBC on the unstructured Sculpture Garden dataset despite using 29% fewer scans in the respective input set. CEBC and EBC perform similarly on the structured Office Loop dataset again despite CEBC using 26% fewer scans in the input set.

The informativeness of distilled maps is measured using overlap percentage with a dense map, where overlapping points are within 0.5 m. Dense maps are generated for all results by combining 250 scans then applying a 0.5 m voxel filter to ensure dense maps evenly distributed points. The unique descriptor distance used to generate the reduced input set is  $\mathcal{E} = 0.025$ , sorted set size factor is  $F = 10$ , and the distance radius for the pose-based CEBC approximation function is  $\alpha = 15$  across all results. The descriptor neural network is trained on UCLA campus datasets not used in any results for 30 epochs. A modified variant of [12] with loop closures and custom OptMap interfaces provides LiDAR scans with labeled poses and motion correction. An odometry-only variant without loop closures is available open-source<sup>4</sup>.

#### A. Geometric Map Distillation Reward Function Evaluation

The first experiment compares the informativeness of output maps generated by optimizing multiple submodular map distillation functions. Two custom datasets were collected for this result, the semi-urban outdoor Sculpture Garden and the urban outdoor Office Loop. Output maps were made by optimizing four functions from Section IV: the descriptor-based coverage function (Desc. Coverage (7)), descriptor-based clustering functions (CEBC (11) using reduced input set and EBC (9)), and an optimal function which directly selects scans to maximize overlap with the dense map. The number of scans used in outputs maps was increased until any suboptimal reward function exceeded 50% overlap. The optimal function was provided the dense map used for evaluation and selected scans which would maximize overlap percent, and required several hours to produce output maps due to the large input sets and density of point cloud data. All reward functions were optimized using the greedy algorithm.

<sup>4</sup>Modified version of DLIO [12] for OptMap: [https://github.com/vecr-ucla/direct\\_lidar\\_inertial\\_odometry/tree/feature/optmap](https://github.com/vecr-ucla/direct_lidar_inertial_odometry/tree/feature/optmap)

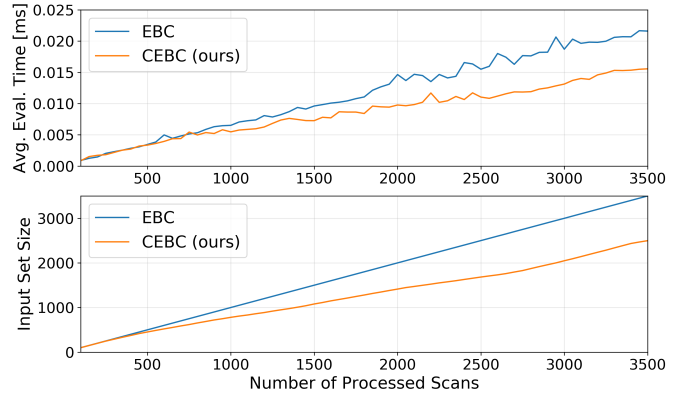


Fig. 8: Average function evaluation time and input set size for Sculpture Garden dataset. The function evaluation time scales with the size of the input set, which is smaller for CEBC due to the reduced set filtering which eliminates sequentially redundant elements of the input set.

Results from the first experiment are seen in Fig. 7 where CEBC and EBC generate maps that are nearly as informative as the optimal function, and significantly outperform descriptor coverage. Overlap percentages for the Sculpture Garden were 37%, 48%, 53%, and 58% for descriptor coverage, CEBC, EBC, and the optimal function respectively. Overlap for the Office Loop was 50%, 56%, 54%, and 70% for the four functions, respectively. The descriptor coverage function fails to distinguish between outliers and informative scans, which leads to poor performance on the semi-structured Sculpture Garden dataset because learned descriptors are known to perform better in structured environments [57]. Both clustering functions outperform coverage in both datasets and achieve near-optimal performance. The marginal performance gain of EBC over CEBC in the Sculpture Garden dataset is attributed to the fact that CEBC uses the reduced input set and therefore has limited solution options. As will be discussed next, any small potential performance loss of CEBC is accompanied by improvements in other performance metrics.

The defining distinction between CEBC and EBC is that the former uses a reduced input set. A direct consequence of this is the immediate improvement in function evaluation times, as shown in Fig. 8. For the final optimization in the Sculpture Garden, a 33% reduction in the average function evaluation time was observed (top figure). This is a direct result of using fewer set elements: the full input set had 3575 elements and the reduced set had 2528; a 29% reduction (bottom figure). It is clear from Fig. 8 that the reduced input set addresses the primary weakness of clustering functions, namely that the evaluation complexity scales with the size of the input set. From a practical point of view, reducing the input set size enables the proposed approach to be used on larger datasets (longer data collection) and resource-constrained hardware.

#### B. Distillation Effectiveness Ablation Study

The second experiment highlights the benefits of dynamic reordering and compares the relative strengths and weaknesses of multiple approximation functions used to generate ordering scores. In addition to the approximations presented in Section V-C (the pairwise information descriptor approximation (16) and heuristic pose approximation (13)), we also evaluate a



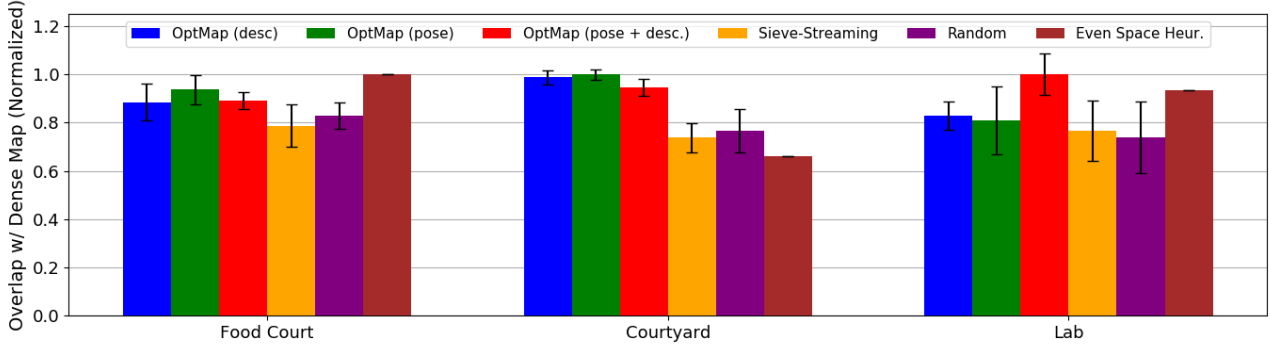


Fig. 9: Percent of overlap from dense map to output map for ablation test on Food Court, Courtyard, and Lab datasets shown in Fig. 10. Results are normalized by the highest scoring method for each dataset. Food court maps made with four scans, Courtyard maps made with twelve scans, and Lab maps made with eight scans. All bars are the average overlap with the dense maps from Fig. 10 with standard deviation shown with whiskers.

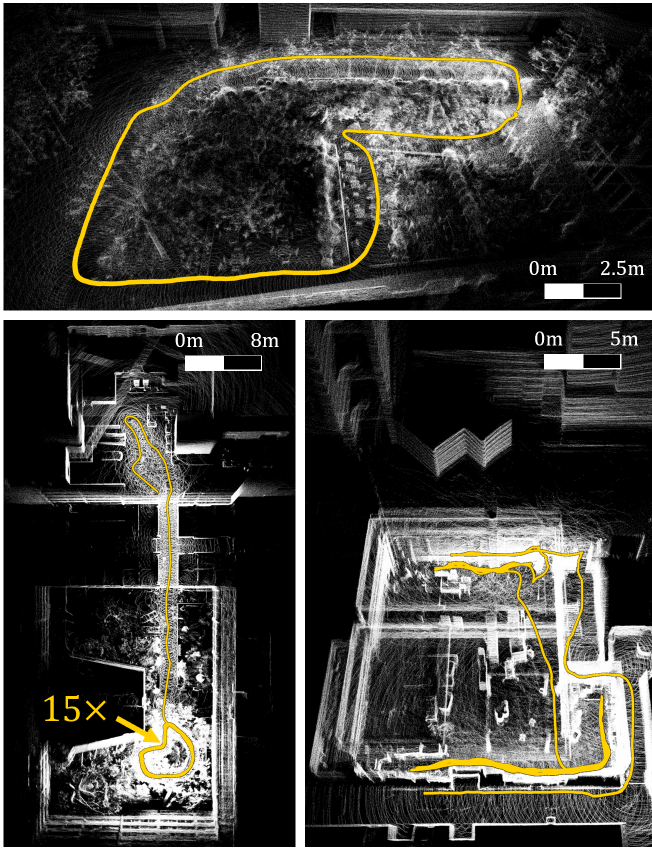


Fig. 10: Dense maps used for Fig. 9. Each map is made from 250 scans, with the sensor trajectory indicated by the yellow path. Top is Food Court (32-beam OS1), an outdoor food court with structured pathways and seating. Bottom-left is Courtyard (32-beam OS0) which entails fifteen loops of an outdoor courtyard followed by a single mapping pass through tight corridors and an adjacent alley in the figure top. Bottom-right is Lab (32-beam OS0) which contains multiple mapping passes capturing the interior of a large lab space and a single pass captured the outdoor alley and nearby tight hallways.

third approximation, which takes the sum of both the pairwise information descriptor and pose approximations. An ablation study compares OptMap using these three approximation functions with the baseline Sieve-Streaming algorithm, random element selection, and the heuristic solution with even spacing described by Algorithm 6. Sieve-Streaming is OptMap with no dynamic reordering but has identical initial solution value bounds. All methods use input sets filtered by Algorithm 2.

Each optimization method generated ten distilled maps on three custom datasets collected at UCLA with dense maps shown in Fig. 10. The Food Court dataset (top figure) is a short loop where all scans are evenly spaced and the sensor never mapped the same area multiple times. The Courtyard (bottom-left figure) introduces a bias to the input set by repeating a small loop fifteen times before making a single mapping pass away from the loop. The bias in the input set is the result of the loop being significantly overrepresented, with the loop accounting for 86% of collected scans but only 31% of the unique distance traveled. Finally, the Lab (bottom-right figure) introduces input set bias by mapping the inside south and north walls of a large lab space with four passes each. Lab differs from Courtyard in that the underrepresented portions of its map correspond to single mapping passes located near the indoor trajectories. Specifically, in an alley to the north and a narrow hallway to the south. The output map size for each dataset is hand-picked, with four scans used for Food Court, twelve scans used for Courtyard, and eight scans used for Lab.

The average and standard deviation overlap percentages for all three datasets are presented in Fig. 9. We normalized the results by the highest performing method for each dataset. All methods are expected to perform well on Food Court, with the evenly spaced heuristic achieving the highest average overlap percent. The descriptor, pose, and combined dynamic reordering methods have normalized average overlaps of 88.5%, 93.6%, and 89.2%, with normalized standard deviations of 7.6%, 5.9%, and 3.6% respectively. Sieve-Streaming has a normalized average overlap of 78.7% and standard deviation of 8.7%, and random has an average overlap of 83% and standard deviation of 5.5%. As with all three datasets, the dynamic reordering methods outperform Sieve-Streaming and random selection because the approximation functions effectively guide the optimization. Notably, a CEBC score of 0.5 (1/2 of optimal) is achieved in Food Court using only one scan in all cases because it is such a small dataset. This indicates that dynamic reordering improved the average normalized overlap by 9.8%-14.9% over Sieve-Streaming, primarily due to the guidance provided by the approximation functions. Because the 1/2-suboptimality bound is exceeded in all three datasets within only 1-3 scans, Sieve-Streaming performs similarly to random selection in all cases.

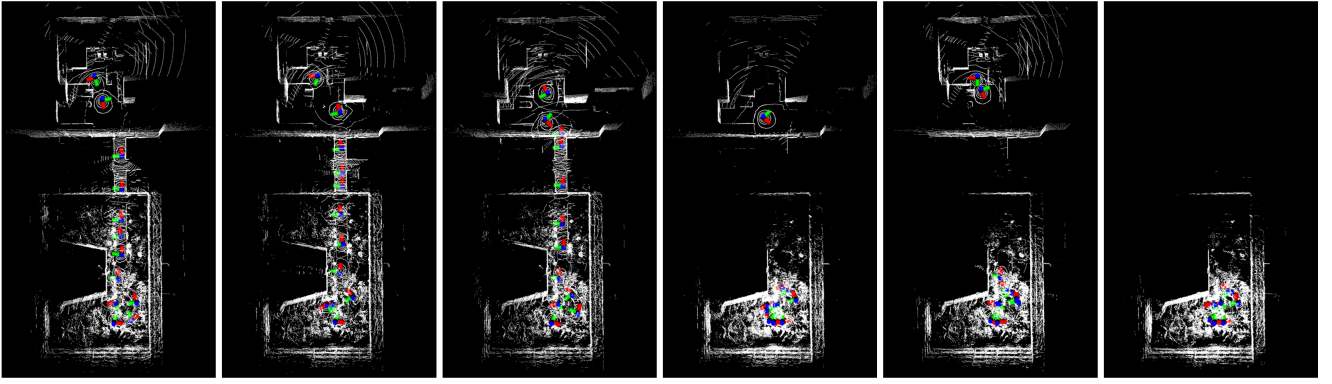


Fig. 11: Sample output maps using different methods from Fig. 9. Methods from left to right are OptMap with descriptor-based dynamic reordering, OptMap with pose-based dynamic reordering, OptMap with both descriptor and pose dynamic reordering, Sieve-Streaming, random selection, and the evenly spaced heuristic. Dynamic reordering methods capture the entire map where the other three methods only select scans from the loop seen at the bottom of each map.

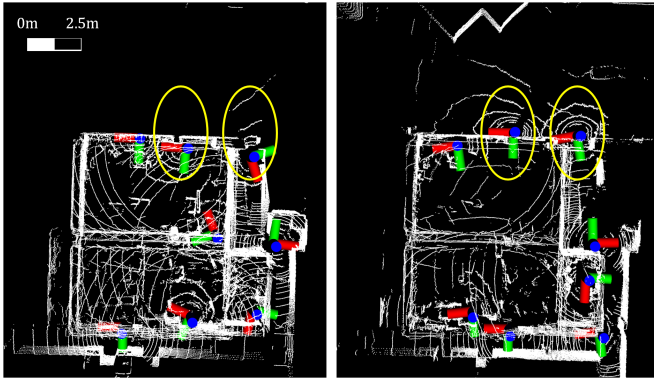


Fig. 12: The pose-based dynamic reordering is unable to accurately select the highest value elements in cases where nearby scans capture significantly different environments. These two maps from the Lab dataset (Fig. 9) were generated using the same pose-based approximation dynamic reordering method, and demonstrate the large standard deviation from the pose-based dynamic reordering as scans are arbitrarily selected from one side of the wall (yellow ovals) leading to occasional suboptimal results.

Courtyard is meant to demonstrate the strengths of dynamic reordering, which are emphasized by the visual results presented in Fig. 11. The first three panels of Fig. 11 are representative maps from the descriptor, pose, and combined dynamic reordering methods where multiple scans and sufficient coverage of the single pass are present for all three methods. The final three panels show representative maps from Sieve-Streaming, random, and the evenly spaced heuristic; each contain very few scans and minimal coverage from the single pass. The qualitative results match the overlap and standard deviations presented in Fig. 9. The average normalized overlap for the dynamically reordered methods is 98.8%, 100%, and 94.7%, and the average normalized standard deviation is 3%, 2.2%, and 3.4%. In contrast, the average normalized overlap for Sieve-Streaming, random, and the evenly spaced heuristic is 73.8%, 76.8%, and 66%. The average normalized standard deviation for Sieve-Streaming and random are 6.1% and 9.1%. Both Fig. 11 and Fig. 9 show that dynamic reordering is particularly valuable when an input set contains redundantly mapped areas. Note that in the context of field operations, the value of dynamic reordering is most apparent in providing a summary map when a robot has patrolled the same general area many times, but then explores a new environment, i.e., a patrol task followed by reconnaissance task.

The Lab dataset highlights the strengths of the pairwise information descriptor approximation for dynamic reordering, as it preserves scene context when scans from different environments are collected in close proximity. The average normalized overlap percent for the descriptor- and pose-based dynamic reordering methods are similar at 82.9% and 80.8% respectively. However, the pose approximation is significantly less reliable as the normalized standard deviations are 5.8% and 14%; an increase of 240%. The inconsistency of the pose approximation is demonstrated qualitatively in Fig. 12 where the left figure shows a failed map with insufficient coverage of the alley to the north. The pose approximation cannot distinguish between scans taken on either side of the wall, meaning several maps fail to include scans in the alley on the north or hallway on the south. While the descriptor approximation slightly outperforms the pose approximation, the strongest result comes from the combined approximation. This is because the pose approximation successfully encourages scan placement diversity while the descriptor approximation effectively differentiates distinct scans from similar locations.

### C. Real-Time Map Summarization Evaluation

In this final experiment, we demonstrate OptMap’s minimal computation requirements when summarizing large datasets. Summarizing long-duration mapping sessions is both one of the most useful applications of OptMap and the most computationally challenging, because the evaluation complexity of CEBC scales with the size of the input set. By presenting the time required to find a solution and return actionable maps, we highlight OptMap’s real-time map distillation capability in the most challenging scenarios. For this experiment, we summarize three smaller datasets, including the Oxford Spires Observatory Quarter Sequence 1 and 3 collected on a Hesai QT64 LiDAR [58], and Semantic KITTI sequence 10 collected on a Velodyne HDL-64E LiDAR [59] using distilled maps with 25, 50, and 100 scans. Three larger datasets are summarized with 100, 250, and 500 scans and include Semantic KITTI sequence 02, Newer College Dataset Long Experiment collected on a 64-beam Ouster OS1 LiDAR [60], and a custom dataset called Forest Loop which was collected using a 128-beam OS1 LiDAR through a mostly unstructured forest environment. The two largest datasets used in this experiment are the Newer

TABLE I: OptMap computation time results. Left column gives the dataset, where sequences from three standardized datasets were chosen alongside one custom dataset collected on a 128-beam Ouster OS1 LiDAR (Forest Loop pictured in Fig. 15). Distilled map size indicates how many scans were used to generate the map, optimization time is the time from function call to when the solution set is selected, and load time is the remaining time spent loading point clouds from storage to computer memory.

Dataset (Num. Scans)	Distilled Map Size	Opt. Time [ms]	Load Time [ms]	Total Time [ms]
Oxford Spires Obs. Quarter Seq. 1 [58] (4,052 scans)	25	24.4	27.2	<b>51.4</b>
	50	29.0	62.3	<b>91.3</b>
	100	45.0	123.0	<b>168.1</b>
Oxford Spires Blenheim Palace Seq. 3 [58] (6,970 scans)	25	26.0	39.5	<b>60.5</b>
	50	30.9	59.1	<b>90.0</b>
	100	48.9	132.8	<b>181.7</b>
Semantic KITTI 10 [59] (1,224 scans)	25	12.6	77.9	<b>90.5</b>
	50	19.3	140.3	<b>159.6</b>
	100	30.3	280.4	<b>310.7</b>
Semantic KITTI 02 [59] (4,663 scans)	100	36.6	291.4	<b>328.0</b>
	250	61.7	785.4	<b>847.1</b>
	500	190.8	1507.3	<b>1698.1</b>
Newer College Long Experiment [60] (26,559 scans)	100	245.0	195.5	<b>440.5</b>
	250	602.3	535.8	<b>1138.1</b>
	500	1159.7	962.7	<b>2122.4</b>
Forest Loop (34,158 scans)	100	231.1	621.2	<b>852.3</b>
	250	639.7	1626.6	<b>2266.3</b>
	500	663.1	3138.8	<b>3801.9</b>

College Dataset Long Experiment [60] and the Forest Loop, which contain 26,559 and 34,158 scans representing 44 and 28.5 minutes (or 18.6 and 34 GB) of continuous LiDAR mapping respectively. For each result configuration, OptMap was run five times and experienced negligible variation in either the optimization or map loading time.

The optimization, map loading, and total times for all six datasets are presented in Table I, where the primary result to highlight is the linear or sublinear growth of return time with respect to distilled map size across all experiments. One of the most appealing properties of streaming submodular maximization (and thus OptMap) is that the optimization time scales sublinearly with the solution set size (Proposition 1), as demonstrated across all datasets. The map load time grows linearly with the size of the distilled map as exhibited in each experiment. The notable difference in load times between experiments is attributable to the density of each LiDAR sensor. For example, the 128-beam used to collect Forest Loop captures over 260,000 points in each scan, and accordingly has the highest average load time of 6.3 ms per scan.

Summarization is a key application for OptMap, with visual results presented in Figs. 13 to 15. Figure 13 demonstrates generating summary maps with flexible size and resolution on-the-fly that could be used, e.g., for efficient map communication or global place recognition. Figure 14 shows a high-fidelity and extremely detailed map of the Newer College Dataset Long Experiment generated by OptMap. The inset shows a detailed map that is not usually available from LiDAR SLAM in real-time due to the computation and memory load required for maintaining dense maps. Finally, Fig. 15 shows the largest OptMap distilled map by number of input scans. It also highlights the use of position and time constraints described

in Section VI-C, as the inset shows the location used to generate the motion planning map shown in Fig. 1a. Although this result focuses on map summarization, we envision many applications of OptMap that utilize real-time map distillation alongside flexible position and time constraints to enhance existing autonomy algorithms and operator awareness.

## VIII. CONCLUSION

This work presented OptMap, a real-time geometric map distillation algorithm that can generate provably near-optimal representative distillation maps from large datasets of aligned scans. We propose multiple theoretical and algorithm innovations which both provide a means for quantifying informativeness in geometric maps, and allows for the efficient optimization of such maps. The novel submodular reward function Continuous Exemplar-Based Clustering (CEBC) effectively rewards informativeness in the form of map overlap with the ability to significantly reduce the size of input sets and improve computation time via the elimination of sequentially redundant elements. Dynamic reordering is a novel addition to streaming submodular maximization algorithms, which uses several developed approximation functions for CEBC to address multiple sources of input order bias. A parallel optimization and map loading scheme further reduces computation times, alongside multiple algorithmic innovations such as tight initial bounds and the ability to add position and time constraints. The results demonstrate the efficacy of CEBC and dynamic reordering across a range of custom LiDAR datasets, and the minimal computation times required by OptMap for summarizing large open-source datasets. We envision many practical applications of OptMap that utilize the



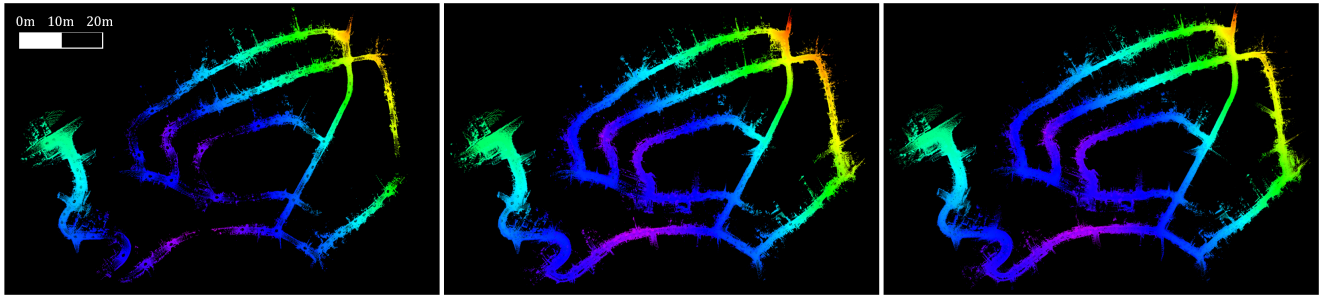


Fig. 13: Output OptMap maps for Semantic KITTI 02 with 100, 250, and 500 scans. Color indicates z-coordinate of point. OptMap is capable of generating map summaries with flexible size and resolution for autonomous planning at various scales.

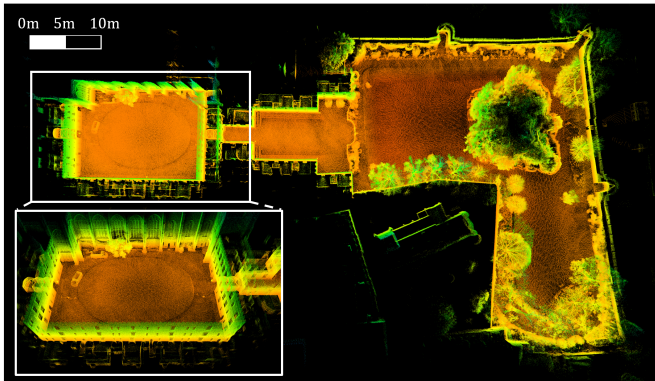


Fig. 14: 250 scan output OptMap map from Newer College Dataset Long. Color indicates z-coordinate of point. Inset box shows the level of detail and geometric map consistency which OptMap can produce. Maps with similar level of detail are difficult to maintain in online SLAM due to memory or computation time constraints.

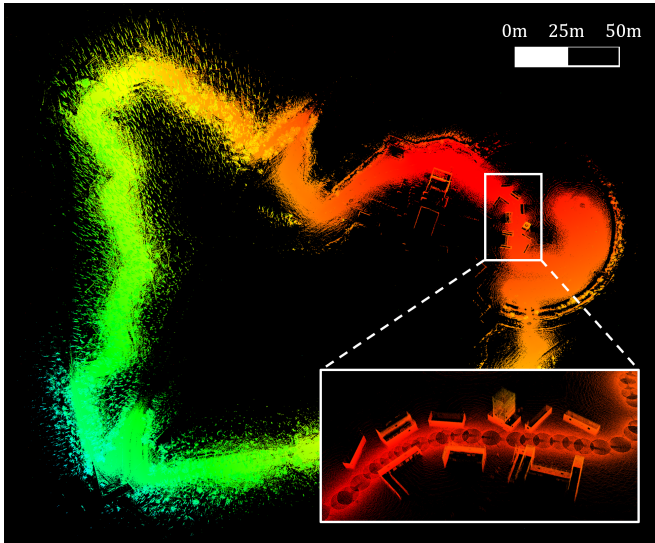


Fig. 15: 500 scan output OptMap map from custom forest loop dataset. Color indicates z-coordinate of point. Forest loop dataset covers 2.6 km and collects 34,158 scans. Inset box shows the level of detail around several buildings.

ability to specify map position and density in order to enhance and enable robotic autonomy algorithms.

Future work on OptMap can incorporate higher quality learned descriptors and other similarity metrics for improved distillation results across a wider variety of environments. Additional work in generalizing dynamic reordering could yield a novel generalized streaming submodular maximization algorithm that uses limited *a priori* information to address

significant forms of input order bias in computationally efficient methods. Further, developing additional reward functions could result in algorithm variants that accurately distill *user prompted* sets of geometric information from large datasets. Improved functionality could also be derived from general matroid constraints. For example, a knapsack constraint could enable input sets with multiple contributing sensor types, and set coverage constraints could allow for minimum size solutions which satisfy a defined coverage criterion. Such innovations can lead to a tighter, bidirectional integration between geometric mapping and the downstream autonomy algorithms or operators that rely on compact and informative geometric maps.

## REFERENCES

- [1] J. Ma, J. Zhang, J. Xu, R. Ai, W. Gu, and X. Chen, "Overlaptransformer: An efficient and yaw-angle-invariant transformer network for lidar-based place recognition," *IEEE Robotics and Automation Letters*, vol. 7, no. 3, pp. 6958–6965, 2022.
- [2] X. Chen, T. Läbe, A. Milioto, T. Röhling, J. Behley, and C. Stachniss, "Overlapnet: A siamese network for computing lidar scan similarity with applications to loop closing and localization," *Autonomous Robots*, pp. 1–21, 2022.
- [3] J. Arce, N. Vödisch, D. Cattaneo, W. Burgard, and A. Valada, "Padloc: Lidar-based deep loop closure detection and registration using panoptic attention," *IEEE Robotics and Automation Letters*, vol. 8, no. 3, pp. 1319–1326, 2023.
- [4] J. Komorowski, "Minkloc3d: Point cloud based large-scale place recognition," in *Proceedings of the IEEE/CVF Winter Conference on Applications of Computer Vision*, 2021, pp. 1790–1799.
- [5] D. Thorne, N. Chan, Y. Ma, C. S. Robison, P. R. Osteen, and B. T. Lopez, "Submodular optimization for keyframe selection & usage in slam," in *2025 IEEE International Conference on Robotics and Automation (ICRA)*. IEEE, 2025, pp. 5033–5039.
- [6] G. L. Nemhauser, L. A. Wolsey, and M. L. Fisher, "An analysis of approximations for maximizing submodular set functions—i," *Mathematical programming*, vol. 14, pp. 265–294, 1978.
- [7] G. L. Nemhauser and L. A. Wolsey, "Best algorithms for approximating the maximum of a submodular set function," *Mathematics of operations research*, vol. 3, no. 3, pp. 177–188, 1978.
- [8] A. Badanidiyuru, B. Mirzasoleiman, A. Karbasi, and A. Krause, "Streaming submodular maximization: Massive data summarization on the fly," in *Proceedings of the 20th ACM SIGKDD International Conference on Knowledge Discovery and Data Mining*, 2014, pp. 671–680.
- [9] C. Chekuri, S. Gupta, and K. Quanrud, "Streaming algorithms for submodular function maximization," in *Automata, Languages, and Programming: 42nd International Colloquium, ICALP 2015, Kyoto, Japan, July 6–10, 2015, Proceedings, Part I* 42. Springer, 2015, pp. 318–330.
- [10] M. Feldman, A. Karbasi, and E. Kazemi, "Do less, get more: Streaming submodular maximization with subsampling," *Advances in Neural Information Processing Systems*, vol. 31, 2018.
- [11] E. Kazemi, M. Mitrovic, M. Zadimoghaddam, S. Lattanzi, and A. Karbasi, "Submodular streaming in all its glory: Tight approximation, minimum memory and low adaptive complexity," in *International Conference on Machine Learning*. PMLR, 2019, pp. 3311–3320.

- [12] K. Chen, R. Nemiroff, and B. T. Lopez, "Direct lidar-inertial odometry: Lightweight lio with continuous-time motion correction," in *2023 IEEE International Conference on Robotics and Automation (ICRA)*. IEEE, 2023, pp. 3983–3989.
- [13] L. Carlone, A. Kim, T. Barfoot, D. Cremers, and F. Dellaert, Eds., *SLAM Handbook. From Localization and Mapping to Spatial Intelligence*. Cambridge University Press, 2025.
- [14] Y. Cai, W. Xu, and F. Zhang, "ikd-tree: An incremental kd tree for robotic applications," *arXiv preprint arXiv:2102.10808*, 2021.
- [15] W. Xu, Y. Cai, D. He, J. Lin, and F. Zhang, "Fast-lio2: Fast direct lidar-inertial odometry," *IEEE Transactions on Robotics*, vol. 38, no. 4, pp. 2053–2073, 2022.
- [16] J. Zhang, S. Singh *et al.*, "Loam: Lidar odometry and mapping in real-time," in *Robotics: Science and Systems*, vol. 2, no. 9. Berkeley, CA, 2014, pp. 1–9.
- [17] T. Shan, B. Englot, D. Meyers, W. Wang, C. Ratti, and D. Rus, "Lio-sam: Tightly-coupled lidar inertial odometry via smoothing and mapping," in *2020 IEEE/RSJ International Conference on Intelligent Robots and Systems (IROS)*. IEEE, 2020, pp. 5135–5142.
- [18] A. Hornung, K. M. Wurm, M. Bennewitz, C. Stachniss, and W. Burgard, "OctoMap: An efficient probabilistic 3D mapping framework based on octrees," *Autonomous Robots*, 2013. [Online]. Available: <https://octomap.github.io>
- [19] Y. Yue, P. N. Senarathne, C. Yang, J. Zhang, M. Wen, and D. Wang, "Hierarchical probabilistic fusion framework for matching and merging of 3-d occupancy maps," *IEEE Sensors Journal*, vol. 18, no. 21, pp. 8933–8949, 2018.
- [20] Y. Yue, C. Yang, Y. Wang, P. C. N. Senarathne, J. Zhang, M. Wen, and D. Wang, "A multilevel fusion system for multirobot 3-d mapping using heterogeneous sensors," *IEEE Systems Journal*, vol. 14, no. 1, pp. 1341–1352, 2019.
- [21] S. Garg, N. Sünderhauf, F. Dayoub, D. Morrison, A. Cosgun, G. Carneiro, Q. Wu, T.-J. Chin, I. Reid, S. Gould *et al.*, "Semantics for robotic mapping, perception and interaction: A survey," *Foundations and Trends® in Robotics*, vol. 8, no. 1–2, pp. 1–224, 2020.
- [22] Y. Cai, F. Kong, Y. Ren, F. Zhu, J. Lin, and F. Zhang, "Occupancy grid mapping without ray-casting for high-resolution lidar sensors," *IEEE Transactions on Robotics*, 2023.
- [23] S.-K. Kim, A. Bouman, G. Salhotra, D. D. Fan, K. Otsu, J. Burdick, and A.-a. Agha-mohammadi, "Plgrim: Hierarchical value learning for large-scale exploration in unknown environments," in *Proceedings of the International Conference on Automated Planning and Scheduling*, vol. 31, 2021, pp. 652–662.
- [24] K. P. Cop, P. V. Borges, and R. Dubé, "Delight: An efficient descriptor for global localisation using lidar intensities," in *2018 IEEE International Conference on Robotics and Automation (ICRA)*. IEEE, 2018, pp. 3653–3660.
- [25] M. Minoux, "Accelerated greedy algorithms for maximizing submodular set functions," in *Optimization Techniques: Proceedings of the 8th IFIP Conference on Optimization Techniques Würzburg, September 5–9, 1977*. Springer, 2005, pp. 234–243.
- [26] B. Mirzasoleiman, A. Badanidiyuru, A. Karbasi, J. Vondrák, and A. Krause, "Lazier than lazy greedy," in *Proceedings of the AAAI Conference on Artificial Intelligence*, vol. 29, no. 1, 2015.
- [27] B. Mirzasoleiman, A. Badanidiyuru, and A. Karbasi, "Fast constrained submodular maximization: Personalized data summarization," in *International Conference on Machine Learning*. PMLR, 2016, pp. 1358–1367.
- [28] U. Feige, V. S. Mirrokni, and J. Vondrák, "Maximizing non-monotone submodular functions," *SIAM Journal on Computing*, vol. 40, no. 4, pp. 1133–1153, 2011.
- [29] A. Gupta, A. Roth, G. Schoenebeck, and K. Talwar, "Constrained non-monotone submodular maximization: Offline and secretary algorithms," in *International Workshop on Internet and Network Economics*. Springer, 2010, pp. 246–257.
- [30] A. Das and D. Kempe, "Submodular meets spectral: greedy algorithms for subset selection, sparse approximation and dictionary selection," in *Proceedings of the 28th International Conference on International Conference on Machine Learning*, 2011, pp. 1057–1064.
- [31] A. Dasgupta, R. Kumar, and S. Ravi, "Summarization through submodularity and dispersion," in *Proceedings of the 51st Annual Meeting of the Association for Computational Linguistics (Volume 1: Long Papers)*, 2013, pp. 1014–1022.
- [32] D. Dueck and B. J. Frey, "Non-metric affinity propagation for unsupervised image categorization," in *2007 IEEE 11th International Conference on Computer Vision*. IEEE, 2007, pp. 1–8.
- [33] K. El-Arini and C. Guestrin, "Beyond keyword search: discovering relevant scientific literature," in *Proceedings of the 17th ACM SIGKDD International conference on Knowledge discovery and data mining*, 2011, pp. 439–447.
- [34] H. Lin and J. Bilmes, "A class of submodular functions for document summarization," in *Proceedings of the 49th annual meeting of the association for computational linguistics: human language technologies*, 2011, pp. 510–520.
- [35] S. Fujishige, *Submodular functions and optimization*. Elsevier, 2005.
- [36] A. Chakrabarti and S. Kale, "Submodular maximization meets streaming: matchings, matroids, and more," *Mathematical Programming*, vol. 154, pp. 225–247, 2015.
- [37] N. Alaluf, A. Ene, M. Feldman, H. L. Nguyen, and A. Suh, "An optimal streaming algorithm for submodular maximization with a cardinality constraint," *Mathematics of Operations Research*, vol. 47, no. 4, pp. 2667–2690, 2022.
- [38] M. El Halabi, S. Mitrović, A. Norouzi-Fard, J. Tardos, and J. M. Tarnawski, "Fairness in streaming submodular maximization: Algorithms and hardness," *Advances in Neural Information Processing Systems*, vol. 33, pp. 13 609–13 622, 2020.
- [39] M. Monemizadeh, "Dynamic submodular maximization," *Advances in Neural Information Processing Systems*, vol. 33, pp. 9806–9817, 2020.
- [40] K. Banihashem, L. Biabani, S. Goudarzi, M. Hajiaghayi, P. Jabbarzade, and M. Monemizadeh, "Dynamic constrained submodular optimization with polylogarithmic update time," in *International Conference on Machine Learning*. PMLR, 2023, pp. 1660–1691.
- [41] X. Chen and B. Peng, "On the complexity of dynamic submodular maximization," in *Proceedings of the 54th Annual ACM SIGACT Symposium on Theory of Computing*, 2022, pp. 1685–1698.
- [42] K. Banihashem, L. Biabani, S. Goudarzi, M. Hajiaghayi, P. Jabbarzade, and M. Monemizadeh, "Dynamic algorithms for matroid submodular maximization," in *Proceedings of the 2024 Annual ACM-SIAM Symposium on Discrete Algorithms (SODA)*. SIAM, 2024, pp. 3485–3533.
- [43] Y. Chen, L. Zhao, Y. Zhang, S. Huang, and G. Dissanayake, "Anchor selection for slam based on graph topology and submodular optimization," *IEEE Transactions on Robotics*, vol. 38, no. 1, pp. 329–350, 2021.
- [44] H. Kretzschmar, C. Stachniss, and G. Grisetti, "Efficient information-theoretic graph pruning for graph-based slam with laser range finders," in *2011 IEEE/RSJ International Conference on Intelligent Robots and Systems*. IEEE, 2011, pp. 865–871.
- [45] K. Khosoussi, M. Giamou, G. S. Sukhatme, S. Huang, G. Dissanayake, and J. P. How, "Reliable graphs for slam," *The International Journal of Robotics Research*, vol. 38, no. 2–3, pp. 260–298, 2019.
- [46] H. Zhang and Y. Vorobeychik, "Submodular optimization with routing constraints," in *Proceedings of the AAAI conference on artificial intelligence*, vol. 30, no. 1, 2016.
- [47] R. Bai, S. Yuan, H. Guo, P. Yin, W.-Y. Yau, and L. Xie, "Multi-robot active graph exploration with reduced pose-slam uncertainty via submodular optimization," in *2024 IEEE/RSJ International Conference on Intelligent Robots and Systems (IROS)*. IEEE, 2024, pp. 10 229–10 236.
- [48] M. Ramesh, F. Imeson, B. Fidan, and S. L. Smith, "Approximate environment decompositions for robot coverage planning using submodular set cover," in *2024 IEEE 63rd Conference on Decision and Control (CDC)*. IEEE, 2024, pp. 7528–7533.
- [49] Y.-S. Li and K.-S. Tseng, "Computation-aware multi-object search in 3d space using submodular tree," in *2024 IEEE International Conference on Robotics and Automation (ICRA)*. IEEE, 2024, pp. 5956–5962.
- [50] M. Corah, C. O'Meadhra, K. Goel, and N. Michael, "Communication-efficient planning and mapping for multi-robot exploration in large environments," *IEEE Robotics and Automation Letters*, vol. 4, no. 2, pp. 1715–1721, 2019.
- [51] M. Corah and N. Michael, "Distributed matroid-constrained submodular maximization for multi-robot exploration: Theory and practice," *Autonomous Robots*, vol. 43, pp. 485–501, 2019.
- [52] B. Ghahesifard and S. L. Smith, "Distributed submodular maximization with limited information," *IEEE Transactions on Control of Network Systems*, vol. 5, no. 4, pp. 1635–1645, 2017.
- [53] L. Carlone and S. Karaman, "Attention and anticipation in fast visual-inertial navigation," *IEEE Transactions on Robotics*, vol. 35, no. 1, pp. 1–20, 2018.
- [54] A. Downie, B. Ghahesifard, and S. L. Smith, "Submodular maximization with limited function access," *IEEE Transactions on Automatic Control*, vol. 68, no. 9, pp. 5522–5535, 2022.
- [55] S. Li, "Concise formulas for the area and volume of a hyperspherical cap," *Asian Journal of Mathematics & Statistics*, vol. 4, no. 1, pp. 66–70, 2010.

- [56] L. Kaufman and P. J. Rousseeuw, *Finding groups in data: an introduction to cluster analysis*. John Wiley & Sons, 2009.
- [57] H. Oh, N. Chebrolu, M. Mattamala, L. Freißmuth, and M. Fallon, “Evaluation and deployment of lidar-based place recognition in dense forests,” in *2024 IEEE/RSJ International Conference on Intelligent Robots and Systems (IROS)*. IEEE, 2024, pp. 12 824–12 831.
- [58] Y. Tao, M. Á. Muñoz-Bañón, L. Zhang, J. Wang, L. F. T. Fu, and M. Fallon, “The oxford spires dataset: Benchmarking large-scale lidar-visual localisation, reconstruction and radiance field methods,” *International Journal of Robotics Research*, 2025.
- [59] J. Behley, M. Garbade, A. Milioto, J. Quenzel, S. Behnke, C. Stachniss, and J. Gall, “SemanticKITTI: A Dataset for Semantic Scene Understanding of LiDAR Sequences,” in *Proc. of the IEEE/CVF International Conf. on Computer Vision (ICCV)*, 2019.
- [60] M. Ramezani, Y. Wang, M. Camurri, D. Wisth, M. Mattamala, and M. Fallon, “The newer college dataset: Handheld lidar, inertial and vision with ground truth,” in *2020 IEEE/RSJ International Conference on Intelligent Robots and Systems (IROS)*, 2020, pp. 4353–4360.